Climatology of Velocity and Temperature Turbulence Statistics Determined from Rawinsonde and ACARS/AMDAR Data

ROD FREHLICH

Cooperative Institute for Research in Environmental Sciences, University of Colorado, and Research Applications Laboratory, National Center for Atmospheric Research, Boulder, Colorado*

ROBERT SHARMAN

Research Applications Laboratory, National Center for Atmospheric Research, Boulder, Colorado

(Manuscript received 5 February 2009, in final form 23 October 2009)

ABSTRACT

The climatology of the spatial structure functions of velocity and temperature for various altitudes (pressure levels) and latitude bands is constructed from the global rawinsonde network and from Aircraft Communications, Addressing, and Reporting System/Aircraft Meteorological Data Relay (ACARS/AMDAR) data for the tropics and Northern Hemisphere. The ACARS/AMDAR data provide very dense coverage of winds and temperature over common commercial aircraft flight tracks and allow computation of structure functions to scales approaching 1 km, while the inclusion of rawinsonde data provides information on larger scales approaching 10 000 km. When taken together these data extend coverage of the spatial statistics of the atmosphere from previous studies to include larger geographic regions, lower altitudes, and a wider range of spatial scales. Simple empirical fits are used to approximate the structure function behavior as a function of altitude and latitude in the Northern Hemisphere. Results produced for spatial scales less than ~2000 km are consistent with previous studies using other data sources. Estimates of the vertical and global horizontal structure of turbulence in terms of eddy dissipation rate ϵ and thermal structure constant C_T^2 are derived from the structure function levels at the smaller scales.

1. Introduction

Climate change studies have traditionally concentrated on the mean statistical properties of atmospheric variables. Early work was based primarily on rawinsonde data (Lorenz 1967; Palmen and Newton 1969) while more recent work uses global numerical weather prediction (NWP) model reanalyses (Hoskins et al. 1989; Kalnay et al. 1996; Uppala et al. 2005) to evaluate long-term global mean statistics (Fil and Dubus 2005; Peters et al. 2008). But other statistical properties of global atmospheric variables, such as long-term energy spectra and spatial correlations, are also of interest. For instance, climatologies of the observed spatial statistics are essential for rigorous evaluation of the effective spatial resolution of NWP models (Frehlich and Sharman 2004, 2008), for correct interpretation of forecast error statistics (Frehlich 2008), and for optimal data assimilation (Frehlich 2006).

In the seminal paper by Nastrom and Gage (1985) it was shown that the average spatial spectrum of atmospheric kinetic energy and temperature obeys a $k^{-5/3}$ behavior from scales of a few kilometers to hundreds of kilometers, transitioning to a roughly k^{-3} behavior at longer wavelengths (k is the one-dimensional horizontal wavenumber). These results were based on measurements from specially instrumented commercial aircraft from the Global Atmospheric Sampling Program (GASP). More recent data from the Measurements of Ozone and Water Vapor by In-Service Airbus Aircraft (MOZAIC) campaign confirmed this behavior (Lindborg 1999; Cho and Lindborg 2001) and it has also been duplicated with high-resolution general circulation models (GCMs) and

* The National Center for Atmospheric Research is sponsored by the National Science Foundation.

Corresponding author address: Rod Frehlich, CIRES, UCB 216, University of Colorado, Boulder, CO 80309.
E-mail: rgf@cires.colorado.edu

DOI: 10.1175/2010JAMC2196.1

mesoscale NWP models (Koshyk and Hamilton 2001; Skamarock 2004; Frehlich and Sharman 2004; Takahashi et al. 2006; Hamilton et al. 2008).

However, the true climatology of the spatial statistics remains uncertain, since the inference from these statistics is somewhat incomplete. The GASP and MOZAIC sampling is limited to commercial aircraft flight tracks and cruising altitudes (9–12 km), and since high turbulent regions are intentionally avoided, the statistics inferred from these observations may be biased low compared to the true climatology. This problem can be avoided using NWP reanalysis data, however, the models suffer from changes in available data and data assimilation techniques (Bengtsson et al. 2004), and from model filtering effects that tend to underrepresent the smallest scales (Skamarock 2004; Frehlich and Sharman 2008).

Here we produce a more complete climatology based on data derived from a combination of global sounding data (SND) for the larger scales and routine automated winds and temperature measurements from a variety of commercial aircraft [Aircraft Communications, Addressing, and Reporting System (ACARS) and the Aircraft Meteorological Data Relay (AMDAR) system] to improve the climatological estimates at the smaller scales. This avoids the problems associated with the use of model data and extends the sampling regions provided by the GASP and MOZAIC data to higher and lower latitudes and altitudes.

Here, the derived climatologies of spatial variability are based on the average shape and level of structure functions computed from pairs of observations of temperature and velocity from rawinsonde and ACARS/AMDAR measurements for various altitudes, latitude bands, seasons, and geographic locations over the Northern Hemisphere. Structure functions are better suited for the analysis of spatial statistics given the unevenly spaced observations available and can easily be converted to spatial spectra (Frehlich and Sharman 2008). Structure functions were used by Lindborg (1999) and Cho and Lindborg (2001), and have been used for other meteorological applications (Buell 1960; Barnes and Lilly 1975; Maddox and Vonder Haar 1979; Gomis and Alonso 1988). Structure functions also permit local estimates of small-scale turbulence (Frehlich and Sharman 2004) based on recent theoretical interpretations of stably stratified turbulence (Lindborg 1999, 2006; Riley and Lindborg 2008).

The remainder of the paper is organized as follows: section 2 describes the data used. Section 3 describes the data analysis techniques and develops empirical fits to the structure functions. Section 4 presents results for different altitudes, regions, and seasons. Section 5 concludes the paper with a discussion and summary and implications for current theories of mesoscale turbulence. However, we do not attempt to explain the observed scalings produced here. This is an active area of research (Cho et al. 1999; Lindborg 1999, 2006; Lindborg and Cho 2001; Tung and Orlando 2003; Tulloch and Smith 2006, 2009; Gkioulekas and Tung 2006; Riley and Lindborg 2008) that is beyond the scope of this paper.

2. Data sources

The rawinsonde network is concentrated over continental areas of the Northern Hemisphere (see Fig. 1.4.2 of Kalnay 2003) where the average spacing between stations is ~300 km. Here we use an archive (http://dss.ucar.edu/datasets/ds353.4/) of all rawinsonde measurements taken over 34 yr (1973–2006) for the standard times of 0000 and 1200 UTC. The measurement errors are ~0.5 K for temperature (Luers 1997) and ~0.5 m s^{-1} in each horizontal velocity component (Jaatinen and Elms 2000).

The ACARS and AMDAR observations of wind and temperature are used for the time period from 1 January 2001 to 31 December 2008. Here we use the term ''AMDAR'' for both of these datasets collectively. The sampling rate varies from as little as 10 s to as much as 30 min and the accuracy of each horizontal wind component is $\sigma_v \approx 1.25$–1.5 m s^{-1} and of temperature is $\sigma_T \approx 0.5$ K (Benjamin et al. 1999; Drüe et al. 2008). The discretization of the AMDAR data is 0.5 m s^{-1} for wind speed, 1° for wind direction, and 0.1–0.2 K for temperature (Benjamin et al. 1999) and therefore the contribution of random discretization error to total instrument error is negligible. All the AMDAR analyses presented here used the Meteorological Assimilation Data Ingest System (MADIS)-formatted archive (see http://madis.noaa.gov/ for more details). Although more extensive than the GASP or MOZAIC datasets, the AMDAR data are still limited to typical commercial aircraft flight paths; however, the coverage is nearly global, and contains measurements taken during takeoffs and landings, and thus should provide sufficient coverage to estimate the climatology as a function of location, altitude, and time of year. Examples of the AMDAR data locations for one day at two different aircraft flight levels (FL; isobaric surfaces) are shown in Fig. 1. The 250-hPa region (224–276 hPa, which corresponds to commercial aircraft flight levels of approximately 32 000–36 000 ft or 9.75–11.0 km MSL) has the highest concentration of data (Fig. 1a). But even the smaller volume of data provided by AMDAR-equipped aircraft during climbs and descents (e.g., the 500-hPa region corresponding to an FL of approximately 18 000 ft or 5.5 km MSL shown in Fig. 1b) provides ample observations for robust

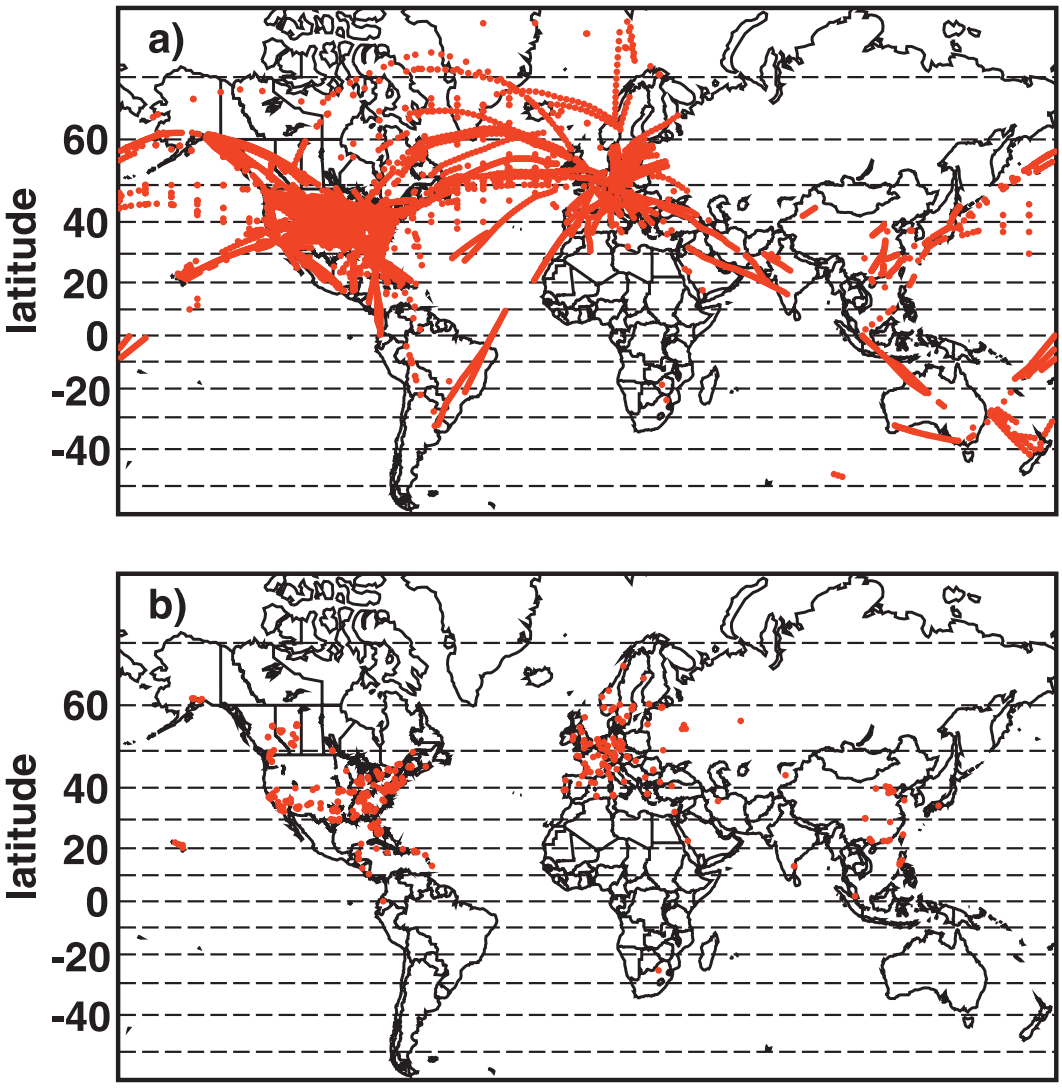

FIG. 1. Location of the AMDAR data that passed all QC checks for the altitude region centered at (a) 250 and (b) 500 hPa for 31 Aug 2008.

determination of spatial statistics when the entire 7-yr observation period is used (from 109 000 measurements per day in 2002 to 212 000 measurements per day in 2007). However, as can be seen in Fig. 1, the AMDAR data are densest over the United States and Europe and therefore, like the rawinsonde network, do not provide a uniform sampling over the globe. Nevertheless, there is still enough coverage over the North Atlantic and North Pacific to construct fairly robust climatologies over most of the Northern Hemisphere.

3. Structure function estimates

For any pair of observation points of variable q separated by a horizontal vector $\mathbf{s}$, the structure function $D_q(\mathbf{s})$ is given by {e.g., Monin and Yaglom [1975, p. 94, Eq. (13.40)]}

$$D_q(\mathbf{s}) = \langle [q(\mathbf{x}+\mathbf{s}) - q(\mathbf{x})]^2 \rangle, \tag{1}$$

where $\langle\ \rangle$ denotes an ensemble average. Figure 2 shows the geometry of the structure function analysis for two-point observations of velocity with east–west velocity component u and north–south velocity component v. Two point observations of temperature share the same geometry. The spatial coordinates of each observation i are given by its spherical coordinates (ϕ_i, λ_i, R_i), where ϕ_i, λ_i, and R_i denote latitude, longitude, and distance from the center of the earth, respectively. Latitude and longitude are expressed in radians and $R_i = R_E + h_i$, where

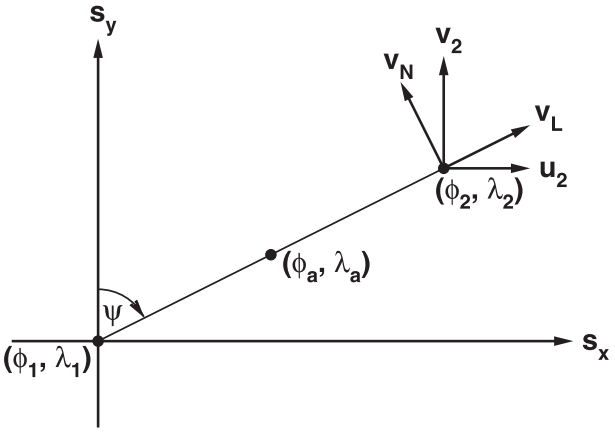

FIG. 2. Geometry for structure function analysis at a given distance R from the center of the earth of two observations at coordinates (ϕ_1, λ_1) and (ϕ_2, λ_2), where ϕ_i and λ_i denote latitude and longitude of observation i, respectively. Here u and v denote the east and north velocity components, respectively; v_L and v_N denote the longitudinal and transverse (normal) velocity components, respectively.

R_E is the radius of the earth and h_i is the altitude (MSL) of the observation.

For rawinsonde data, the latitude and longitude are adjusted for balloon drift using a constant rise rate of 5.0 m s^{-1} (Luers 1997; Luers and Eskridge 1998) and the recorded vector winds. Only rawinsonde data with complete wind speed profiles are used in the analysis to ensure reliable drift calculations. For ease of computation, spatial statistics are calculated on isobaric surfaces defined by the mandatory pressure levels provided in the sounding archive (700, 500, 400, 300, 250, and 200 hPa). The statistics derived for constant pressure surfaces are equivalent to those derived for constant altitude levels (Skamarock 2004).

For each pressure level, the difference between the spatial coordinates of any two observations on the sphere with mean distance from the center of the earth $R = (R_1 + R_2)/2$ is given by the arc distance vector $\mathbf{s} = (s_x, s_y)$ with components defined by (Fig. 2)

$$s_x = R\Delta\lambda \cos\phi_a \quad \text{and} \tag{2}$$

$$s_y = R\Delta\phi, \tag{3}$$

where $\Delta\lambda = \lambda_2 - \lambda_1$, $\Delta\phi = \phi_2 - \phi_1$, and $\phi_a = (\phi_1 + \phi_2)/2$. The arc distance s_x is along constant latitude with positive to the east and s_y is arc distance along constant longitude with positive to the north. The heading ψ of observation 2 with respect to observation 1 is

$$\psi = \tan^{-1}\left(\frac{s_x}{s_y}\right). \tag{4}$$

Structure functions of the velocity field are calculated for the longitudinal component v_L (along the separation vector) and the normal component v_N (normal or transverse to the separation vector), that is,

$$v_L(p, \phi_i, \lambda_i) = u_i \sin\psi + v_i \cos\psi \quad \text{and} \tag{5}$$

$$v_N(p, \phi_i, \lambda_i) = u_i \cos\psi - v_i \sin\psi, \tag{6}$$

where u_i and v_i are the east and north velocity components and p denotes the pressure level. This convention was used by Buell (1960) and other early studies, but other authors have chosen different separation variables and different conventions for the transverse velocity orientation (Lindborg 1999; Cho and Lindborg 2001). However, the structure functions' estimates were found to depend only weakly on the convention used. For example, the difference between this formulation and that of Lindborg (1999) at a separation of 1000 km is less than 3% and at a separation of 400 km is less than 1%.

To ensure a sufficient number of samples for stable results, the velocity and temperature structure functions are computed as averages over longitude bands between $\lambda_{\min}$ and $\lambda_{\max}$ (usually 0°–360°) and within latitude bands $\phi_{\min}$–$\phi_{\max}$ (usually with a bandwidth of 10°). That is, for the velocity structure functions, Eq. (1) is implemented as

$$D_{qq}(p,s) = \frac{1}{M}\sum_{i,j,i\neq j}[v_q(p, \phi_i, \lambda_i) - v_q(p, \phi_j, \lambda_j)]^2, \tag{7}$$

where q is either L or N, and D_{LL} and D_{NN} will denote velocity structure functions throughout, $s = (s_x^2 + s_y^2)^{1/2}$ is the arc distance between the two observations, and M denotes the total number of observation pairs in the latitude band. The separation bin around s is 1/20 of a decade in log space. However, the mean temperature $\overline{T}(p, \phi, \lambda)$ can have a pronounced variation with latitude away from the tropics and must be removed. Therefore, the estimate for the temperature structure function D_T subtracts out the meridionally averaged mean over the latitude band:

$$D_T(p,s) = \frac{1}{M}\sum_{i,j,i\neq j}\{[T(p, \phi_i, \lambda_i) - T(p, \phi_j, \lambda_j)]^2 - [\overline{T}(p, \phi_i) - \overline{T}(p, \phi_j)]^2\}, \tag{8}$$

where

$$\overline{T}(p, \phi) = \frac{1}{M}\sum_{i=1}^{M} T(p, \phi_i, \lambda_i). \tag{9}$$

For D_{LL} and D_{NN}, the 0000 and 1200 UTC sounding data from 1973 to 2006 are used. Since the temperature

sensor from rawinsondes changed after 1988 (Luers and Eskridge 1998), only the time period 1989–2006 is used for the temperature structure functions. The sounding data sample the larger scales and therefore the contribution from the observation error is small compared with the large temperature differences in the atmosphere.

To improve the statistical accuracy of the structure functions from AMDAR data, especially for lower altitudes, each altitude region was divided into 13 pressure intervals of depth 4 hPa for a total extent of 52 hPa centered on each of the mandatory pressure levels of the sounding data (same processing domain as in Fig. 1). The structure functions were calculated for each 4-hPa pressure interval and then averaged to produce a final estimate. Although we assume there are no effects from time differences between soundings taken at different locations, the time difference between the AMDAR observation pairs is restricted to be less than 1 h. This effectively limits the largest separations that can be computed using AMDAR data to ~1000 km. Only data from the *same* aircraft are processed to reduce the contribution of the random bias from different aircraft (Ballish and Kumar 2008; Drüe et al. 2008). This is consistent with the approach used by Lindborg (1999) and Cho and Lindborg (2001), for the GASP and MOZAIC data.

The average structure functions are produced using only sounding data with high-quality flags (''A'' or ''space''). Similarly, only AMDAR data that passed all quality control (QC) stages are used (Moninger et al. 2003). However, examination of the quality controlled AMDAR data showed some remaining inconsistencies between the recorded times and locations for some observation pairs. Therefore, structure functions are produced from AMDAR data pairs only when the effective ground speed, $s/\Delta t$, is between 50 and 400 m s^{-1}. This criterion is based on consideration of typical aircraft airspeeds of 100–250 m s^{-1} and expected maximum head (tail) winds of 50 (150) m s^{-1}.

Examples of the probability density function (PDF) from the rawinsonde and AMDAR data are provided in Figs. 3 and 4. Figure 3 shows the PDF of wind speed and temperature derived from the sounding data. Outliers in the temperature data are clearly evident around the dominant atmospheric feature. There is a small feature above 100 m s^{-1} in the wind speed PDFs. These outliers are removed using a threshold. We also assume that the impact of any remaining bad data (the approximately constant floor of the PDF around the peak) is negligible. This is a good approximation if the total fraction of bad data accepted by the threshold level is small.

For small separations, the structure functions have small values and are sensitive to measurement errors, especially for the AMDAR data. This is demonstrated in Fig. 4 where the tails of the PDF of the velocity differences squared of the AMDAR data appear to deviate from the local scaling in the tails of the distribution. Because of the poor statistical accuracy produced by the small number of events in the extreme tails of the PDF, it is difficult to distinguish legitimate rare events with large horizontal velocity or temperature gradients from random outliers. Thus, in addition to the location and time consistency checks mentioned above, a maximum threshold of 1.5 m s^{-1} km^{-1} was applied to the horizontal wind shear estimates $\Delta u/s$ and $\Delta v/s$ to remove apparently bad wind data. Most of these cases were due to a known error in the AMDAR data wind direction noted by Pauley (2002), and this algorithm successfully removes these errors. Similarly, data with horizontal temperature gradients $\Delta T/s > 0.4$ K km^{-1} were also removed.

Examples of global velocity and temperature structure functions for the AMDAR and sounding data are shown, respectively, in Figs. 5 and 6 for the 250-hPa pressure level at 40°–50°N. Both the velocity and temperature structure functions exhibit the expected $s^{2/3}$ behavior at small lags (equivalent to the $k^{-5/3}$ scaling of spectra at high wavenumber k). The AMDAR temperature data typically intersect the instrument noise floor for spacings less than ≈8 km (not shown), so a minimum separation of 10 km for temperature is used (Fig. 6). However, the velocity data appear to be less noisy at the small scales, and reasonable structure functions are obtained for lags as small as 3 km (Fig. 5). The estimation error is largest for the small lags since they have the smallest number of data pairs; this is clearly shown by the scatter in the sounding structure functions at ~100-km spacing and in the AMDAR velocity structure functions at lags smaller than ~3 km. Nevertheless, the agreement of the AMDAR and sounding structure functions in the overlap regions of ~100–400 km is surprisingly good considering the different spatial and temporal averaging used (see Fig. 1; Kalnay 2003, her Fig. 1.4.2).

For comparison, the Lindborg (1999) average model is also shown in Fig. 5. Note that there is no corresponding model for comparison to the temperature structure functions shown in Fig. 6. The shape of the velocity structure functions is quite consistent with the Lindborg model at all scales, although the AMDAR measurements give levels slightly lower than Lindborg's at the smaller scales. The level of the transverse structure function D_{NN} is higher than the level of the longitudinal structure function D_{LL} at the larger lags (50 km $< s <$ 2000 km), mainly because of the sensitivity of D_{NN} at these larger lags to meridional wind variations induced by planetary waves. Lindborg (1999) has also shown that D_{NN} at lags between 200 and 1000 km is in good agreement with the predictions of 2D

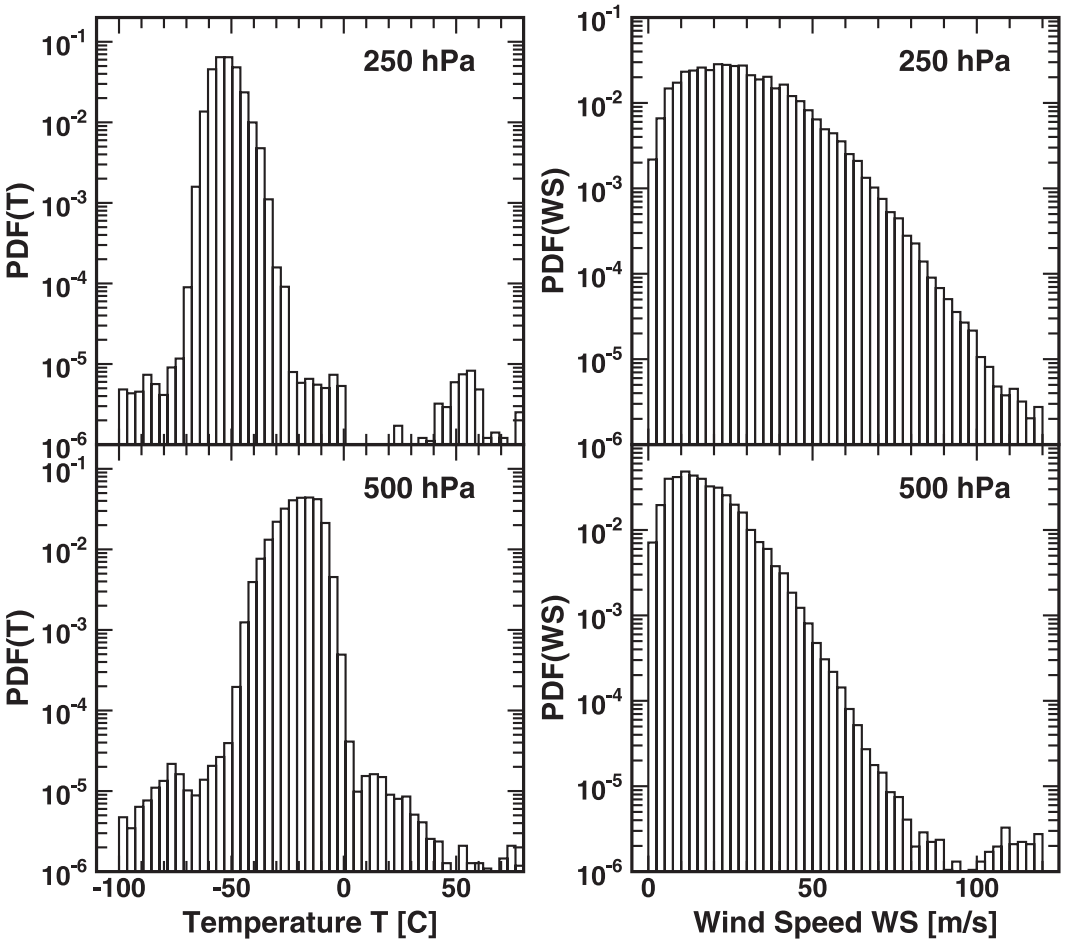

FIG. 3. PDF of temperature and wind speed for all the sounding data from 1973 to 2006 at a latitude band of 40°–50°N and a pressure level of 250 and 500 hPa.

isotropic turbulence based on D_{LL}. At smaller lags, the D_{NN} and D_{LL} merge and consequently, as discussed by Lindborg (1999), neither the 2D isotropic scaling $D_{NN} = {}^{5}/_{3}D_{LL}$ (Ogura 1952; Lindborg 1999) nor the 3D isotropic scaling $D_{NN} = {}^{4}/_{3}D_{LL}$ (Monin and Yaglom 1975, p. 353) are valid.

The ground speed and velocity shear thresholds applied to the AMDAR data were tested by varying the thresholds until little change was produced in the resulting structure functions and the $s^{2/3}$ scaling was consistently observed at small lags. We therefore believe the structure functions presented here are dominated by atmospheric processes and not observation errors, which would produce a constant value at small lags. From the values of the velocity structure function at spacings less than ~2 km in low-turbulence regions, the AMDAR random measurement error is estimated to be less than 0.4 m s^{-1} (see Fig. 5 at small lags). The total measurement error based on differences between two different AMDAR aircraft is difficult to estimate because of the atmospheric contribution. However, we believe the total AMDAR observation error of 1.25–1.5 m s^{-1} per velocity component estimated by Benjamin et al. (1999) and Drüe et al. (2008) may be biased high because of the contribution of atmospheric turbulence.

As shown in Figs. 5 and 6, the structure functions have a simple shape and therefore can be fit to simple empirical models as demonstrated by Lindborg (1999). We use the following empirical model that includes a better representation of the larger scales:

$$D_{\mathrm{mod}}(s) = a_1 s^{2/3}[1 + (s/a_2)^{a_3 - 2/3}]/[1 + (s/a_4)^{a_3}] + \sum_{k=1}^{J} b_k f_k(s) \quad \text{and} \tag{10}$$

$$f_k(s) = [1 - \cos(2\pi s/c_k)] \quad 0 < s < c_k$$
$$= 0 \quad \text{otherwise}, \tag{11}$$

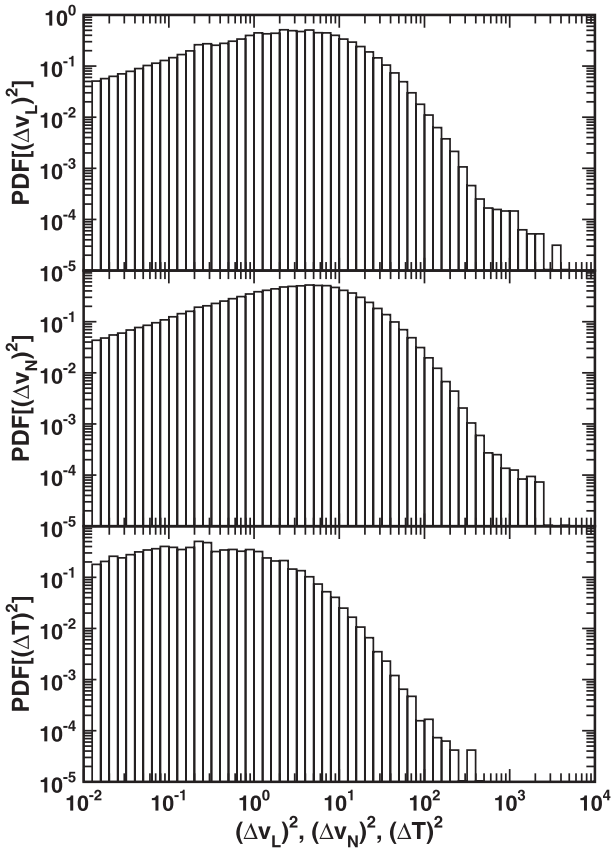

FIG. 4. PDF of the squared differences of longitudinal velocity v_L, transverse velocity v_N, and temperature T at a separation of $s \approx 38$ km for all the AMDAR data in a latitude band of 40°–50°N and a pressure level of 250 hPa.

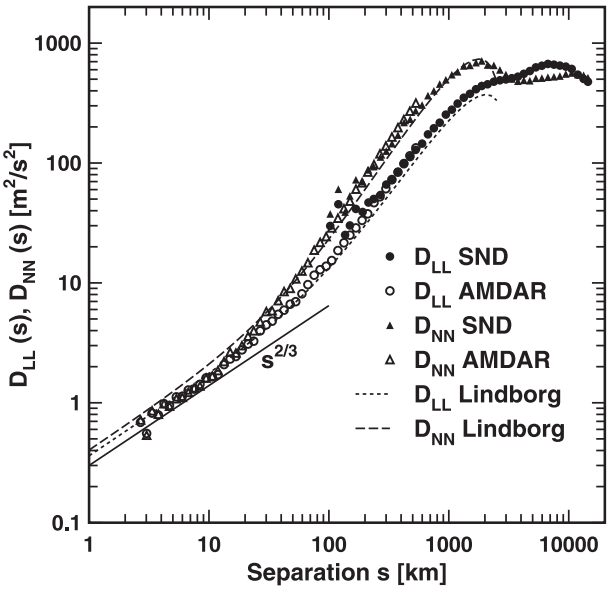

FIG. 5. Velocity structure functions for the AMDAR and SND for the 250-hPa pressure level and latitude band of 40°–50°N. The longitudinal and transverse structure functions are indicated by subscripts *LL* and *NN*, respectively. The theoretical models by Lindborg (1999) and the $s^{2/3}$ scaling law are also shown for comparison.

where k is a wave modal number, J is the number of modes, and mod is LL, NN, or T. The coefficients a_k describe the smaller-scale turbulence while the random amplitudes of the larger-scale planetary waves are modeled by the cosine terms with amplitude b_k and wavelength c_k. This empirical model satisfies the ubiquitous $s^{2/3}$ scaling for small lags and includes the larger-scale planetary waves and baroclinic waves. The deviation from the $s^{2/3}$ scaling to an approximate s^{a_3} scaling occurs at a_2 and for most cases, $a_2 < a_4$, where a_4 defines the largest turbulent scale before planetary waves become important. The tropics and some of the lower altitude regions appear to have a single-scale model (i.e., no planetary-wave component).

The best estimates of the average structure function are produced by combining the information from both the AMDAR and sounding data. We assume that the sounding data provide the best estimate of the larger scales while the AMDAR data provide more accurate small-scale statistics. The best-fit model is therefore produced by minimizing the error

$$e^2 = \sum_{k=1}^{J_A} \ln^2[D_{\mathrm{AMDAR}}(s_k)/D_{\mathrm{mod}}(s_k, a_i)] + \sum_{k=1}^{J_S} \ln^2[D_{\mathrm{SND}}(s_k)/D_{\mathrm{mod}}(s_k, a_i)], \quad (12)$$

where a_i denotes the parameters of the empirical model in Eqs. (10)–(11), J_A is the number of AMDAR estimates, and J_S is the number of sounding estimates. The estimation error of the structure function estimates is proportional to the mean since it is dominated by the turbulent processes (Lenschow et al. 1994). Therefore, the log of the structure function estimates has approximately constant error. Structure function estimates with high estimation errors resulting from small sample sizes are removed by using a threshold based on the relative error, typically 0.04 for the AMDAR data and 0.02 for the sounding data. The Powell algorithm (Press et al. 1986) produces the minimization.

The best-fit models and the structure-function estimates that passed the threshold test are shown in Figs. 7 and 8 for the same region as shown in Figs. 5 and 6, respectively, as well as a lower altitude of 700 hPa. Although these results are for a limited altitude and latitude region, the velocity structure functions agree well with the Lindborg (1999) model. The AMDAR data resolve the $s^{2/3}$ scaling at small scales and the results indicate that the $s^{2/3}$ scaling is valid over a large altitude and spatial

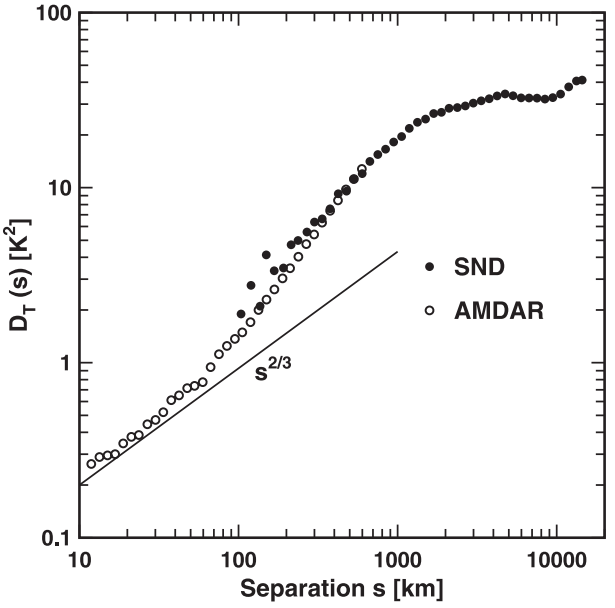

FIG. 6. Temperature structure functions for the AMDAR and SND for the 250-hPa pressure level and latitude band of 40°–50°N. The $s^{2/3}$ scaling law is also shown for comparison.

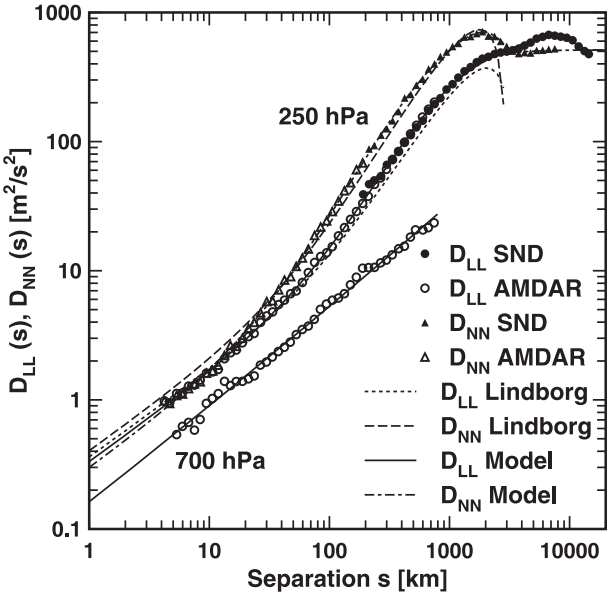

FIG. 7. Best-fit velocity structure functions (Model) for the AMDAR and SND for the 250- and 700-hPa pressure level for the latitude band of 40°–50°N. The results for 700 hPa are shifted lower by a factor of 2. The symbols are the same as in Fig. 5.

region, especially for D_{LL}. The higher level of D_{NN} compared with D_{LL} at 1000-km scales reflects the contributions from planetary and baroclinic waves, especially jet stream loops with typical spacings of 2000 km. Note that like higher altitudes, the levels of the structure function D_{LL} and D_{NN} merge at the smallest spacings. This behavior is consistent with the results of Cho and Lindborg (2001, their Table 2 and their Fig. 5) for the stratosphere.

4. Results

In this section we present some results of the velocity and temperature structure functions (using the parameters in Tables A1–A10 of the appendix) for various global and continental U.S. (CONUS) latitude bands and for various altitudes, seasons, and geographic regions. In Eq. (10), s has units of kilometers and, consequently, a_1 has units of $m^2\ s^{-2}\ km^{-2/3}$, a_2, a_4, and c_i have units of kilometers, a_3 is unitless, and b_i has units of meters squared per second squared. Note that the empirical models for temperature structure functions in Tables A1 and A2 are produced from the AMDAR data only since the results from the sounding data have poor accuracy because of the lack of data in the tropics. We also derive vertical profiles of the turbulence levels, $\epsilon^{2/3}$ and C_T^2, and a geographic distribution of $\epsilon^{2/3}$ at upper levels (250 hPa) in regions where data coverage is adequate. Finally, as an independent check, the velocity and temperature structure functions are compared with the 20-km Rapid Update Cycle (RUC20) NWP-derived structure functions for a limited altitude and latitude band.

a. Structure-function results versus altitude

Examples of the velocity and temperature structure functions at various pressure levels for the 40°–50°N

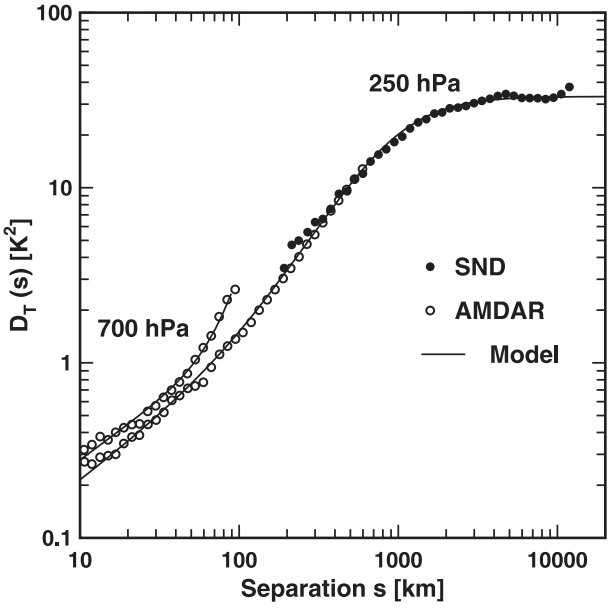

FIG. 8. Best-fit temperature structure function (solid line) from the AMDAR and SND for the 250- and 700-hPa pressure level and latitude band of 40°–50°N.

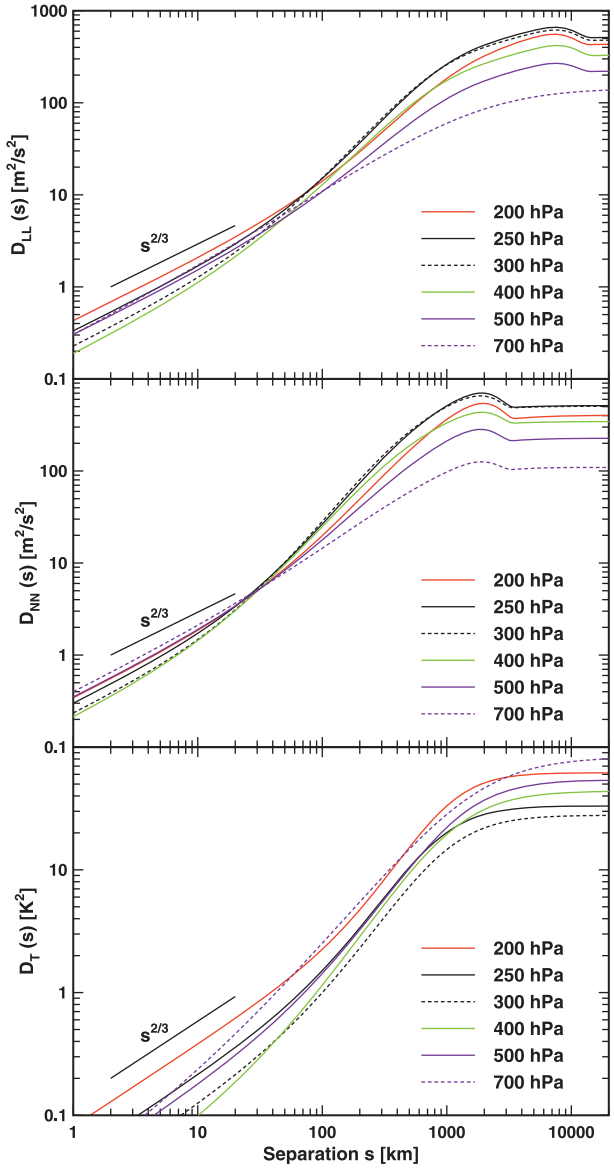

FIG. 9. Best-fit longitudinal-velocity structure functions D_{LL}, transverse-velocity structure functions D_{NN}, and temperature structure functions D_T for the AMDAR and sounding data for the latitude band of 40°–50°N and various pressure levels.

latitude band are shown in Fig. 9. The largest variances are at the 200–300-hPa levels at nearly all scales corresponding to the jet stream maximum at roughly 200 hPa (Koch et al. 2006, their Fig. 1). The mesoscales have similar power but different slopes as a function of altitude. The velocity structure functions show a marked transition in slope at ~100-km separation, consistent with Cho and Lindborg (2001). The smallest scales consistently show the $s^{2/3}$ behavior at all altitudes. For lower altitudes the structure function levels decrease with decreasing altitude for the larger separations s. These results are consistent with Gage and Nastrom (1986). The larger scales show a consistent peak at all altitudes at separations in the 3000–10 000-km range for D_{LL}, with a narrower, more pronounced peak in D_{NN} at ~2000 km or a wavelength of ~4000 km. At this latitude band, the circumference of the earth is approximately 28 000 km, thus the broad maximum in D_{LL} corresponds to planetary waves of zonal wavenumbers 3–5 while the peak in D_{NN} corresponds roughly to zonal wavenumber 7 in agreement with the results of Benton and Kahn (1958).

However, D_T shows a somewhat different behavior. At the largest lags the levels increase with decreasing altitude, except for a large increase at 200 hPa. At smaller lags there is no systematic change in level with altitude. From Hoinka (1998), the annual mean tropopause level for the 40°–50°N latitude band is ~250 hPa. Thus D_T at 200 hPa is mainly in the stratosphere and the increased structure-function level there is consistent with Nastrom and Gage (1985; Tables A1, A2). The transition point is at slightly larger scales (200–300 km) in D_T compared with D_{LL} and D_{NN}. There is no obvious peak in D_T at larger scales, just a slow roll-off starting at ~1000–5000 km. At 500 hPa the roll-off starts at approximately 4000 km or wavenumber 7, in agreement with Julian and Cline (1974) at 40°N.

b. *Structure functions—Latitudinal variations*

Figure 10 shows the latitude dependence of D_{LL}, D_{NN}, and D_T at 250 hPa. The tropical regions below 20°N have the lowest power at all scales, especially for temperature. The power generally increases with latitude, especially for the larger scales, although for spatial scales between approximately 100 and 1000 km the velocity structure functions are nearly independent of latitude above ~30°N. The maximum of D_T is in the 40°–50°N latitude range for all scales. The peak in D_{NN} is observed only in the northern latitudes above 30°N. All these results are consistent with the Nastrom and Gage (1985, their Fig. 8) GASP spectra and Cho and Lindborg (2001, their Fig. 2) velocity structure functions from the MOZAIC tropospheric data. Since our analysis provides information at larger scales, a zonal wavenumber 3 peak is also apparent in the 30°–40°N latitude range. This is consistent with three geographically forced jet maxima climatologically centered at approximately 80°W, 40°E, and 120°E in roughly the 30°–40°N latitude band (Koch et al. 2006, their Fig. 1). However, this feature is only noticeable in D_{NN}. Since it is not evident in D_{LL}, this apparent wavenumber 3 feature could be an artifact of the concentration of data over the continents.

All latitude regions show the ubiquitous $s^{2/3}$ scaling at small separations at this altitude (250 hPa). The transitional scale where the slope of the structure function

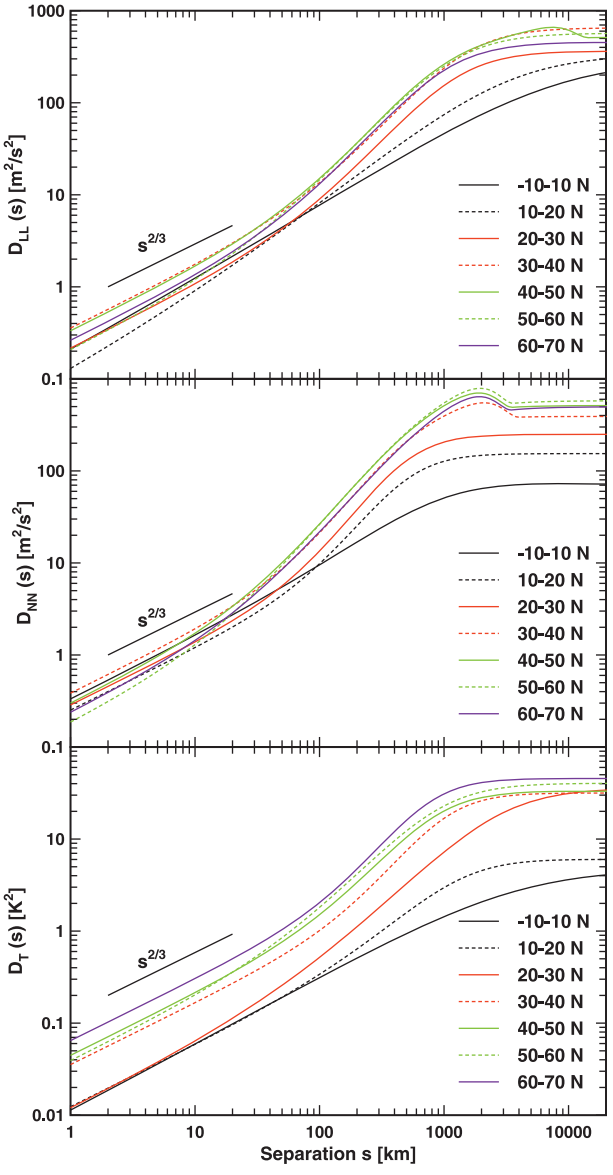

FIG. 10. Best-fit longitudinal-velocity structure functions D_{LL}, transverse-velocity structure functions D_{NN}, and temperature structure functions D_T for the AMDAR and sounding data for 250-hPa pressure level and various latitude bands.

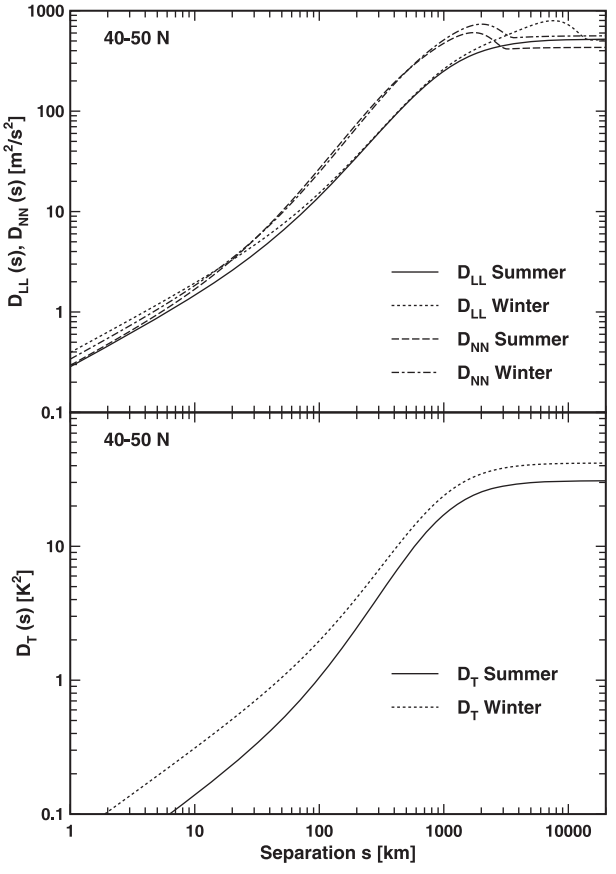

FIG. 11. Best-fit velocity structure functions D_{LL} and D_{NN} and temperature structure functions D_T for the AMDAR and sounding data for 250-hPa pressure level, the latitude band of 40°–50°N, and summer vs winter.

increases from ⅔ is at ~50 km, and is only weakly dependent on latitude except in the tropics where there is no obvious increase in slope. Nastrom and Gage (1985) and Cho and Lindborg (2001) also show only a weak dependence on latitude for the transition scale away from the tropics.

c. *Structure functions—Seasonal variations*

The global structure functions for the 250-hPa pressure level for the summer (June–August) and winter (December–February) seasons for 40°–50°N and 30°–40°N are shown in Figs. 11 and 12. In general, the winter has higher levels at all scales, but this enhancement is especially noticeable in the velocity structure functions at 30°–40°N. The higher levels in this latitude band are consistent with the altitude structure at 40°–50°N described in section 4a and are related to the geographical distribution of jet streams, which is most pronounced in the winter months (Grotjahn 1993, his Fig. 5.7; Koch et al. 2006, their Fig. 4). Enhanced variability at the smaller scales is also observed in the winter months based on pilot reports of turbulence from aircraft (Wolff and Sharman 2008, their Fig. 5) and from global model reanalysis data (Jaeger and Sprenger 2007, their Figs. 1, 2).

Most noticeable is that the peak in D_{NN} at approximately 2000-km separation (zonal wavenumber 7) is apparent only in the winter, reinforcing the notion that this is related to planetary free waves (Benton and Kahn 1958). At both latitudes shown, D_{LL} also has an enhanced component at 8000 km (zonal wavenumber 3) in

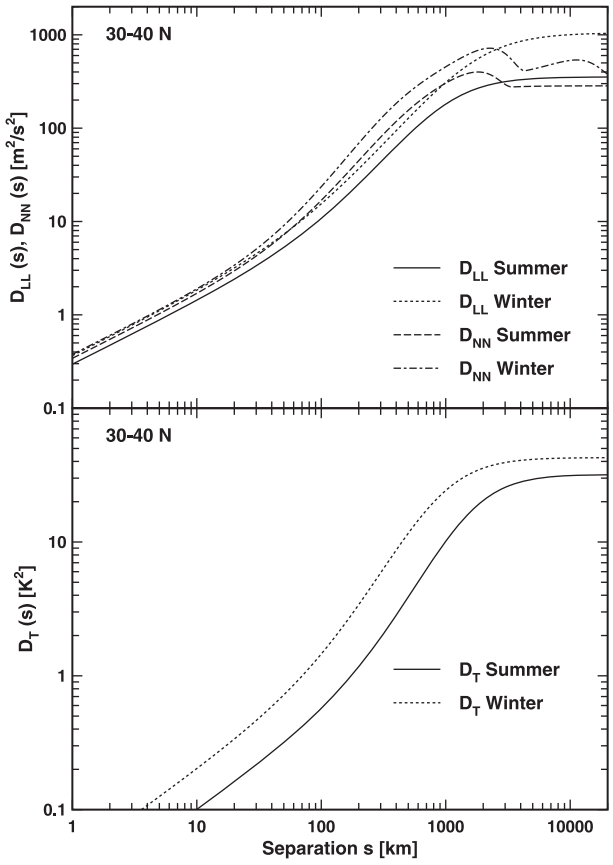

FIG. 12. Best-fit velocity structure functions D_{LL} and D_{NN} and temperature structure functions D_T for the AMDAR and sounding data for 250-hPa pressure level, the latitude band of 30°–40°N, and summer vs winter.

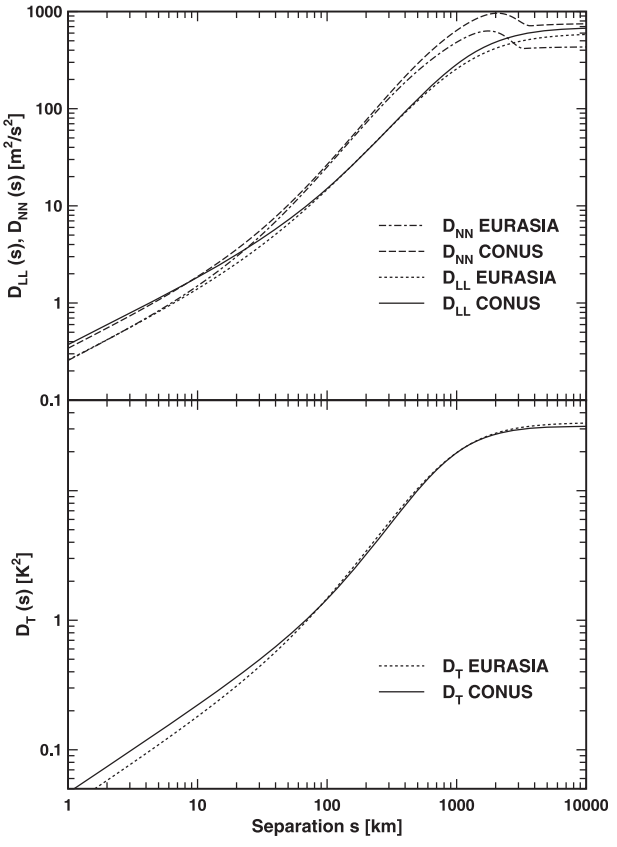

FIG. 13. Best-fit velocity structure functions D_{LL} and D_{NN} and temperature structure functions D_T for the AMDAR and sounding data for 250-hPa pressure level, the latitude band of 40°–50°N, and CONUS vs Eurasia.

the winter, which is most likely related to the wavenumber 3 feature noted above.

d. *Structure functions—Continental variations*

The global velocity and temperature structure functions for 250 hPa and the 40°–50°N latitude band for the continental United States (50°–140°W) and Eurasia (10°W–160°E) are shown in Fig. 13. There is little difference in the temperature statistics at larger scales, but the smaller scales have substantially lower levels over Eurasia than over CONUS. The levels of D_{LL} and D_{NN} also have higher levels over CONUS than over Eurasia at the smaller scales, probably due to enhanced mountain wave activity over the Rocky Mountains in winter and to thunderstorm activity over the eastern half of the United States in summer (Wolff and Sharman 2008), compared to Eurasia. At larger scales D_{NN} has the zonal wavenumber 7 peak mentioned in section 4c, and dominates D_{LL} over both regions. At the largest scales, the CONUS levels are again higher than the Eurasia levels.

e. *Structure functions—Effects of mountains*

The impact of mountainous regions is investigated by selecting two subdomains with a high density of AMDAR data: the Rocky Mountains region (latitude 30°–50°N, longitude 100°–125°W) and the eastern United States (latitude 30°–50°N, longitude 75°–100°W). The comparison of the velocity structure functions is shown in Fig. 14. Note the large enhancement for the mountain (western) region at lags less than 20 km as well as the increase in power of D_{LL} compared to D_{NN}. This behavior has also been observed by similar analysis of research aircraft data (Frehlich and Sharman 2008), and is consistent with Jasperson et al. (1990) and the predictions of elevated turbulence spectra levels dominated by gravity waves (Cho et al. 1999; Lindborg 2007).

f. *Profiles of small-scale turbulence*

Recent theoretical and experimental results for stably stratified anisotropic turbulence (Lindborg 1999, 2006; Cho and Lindborg 2001; Riley and Lindborg 2008) have

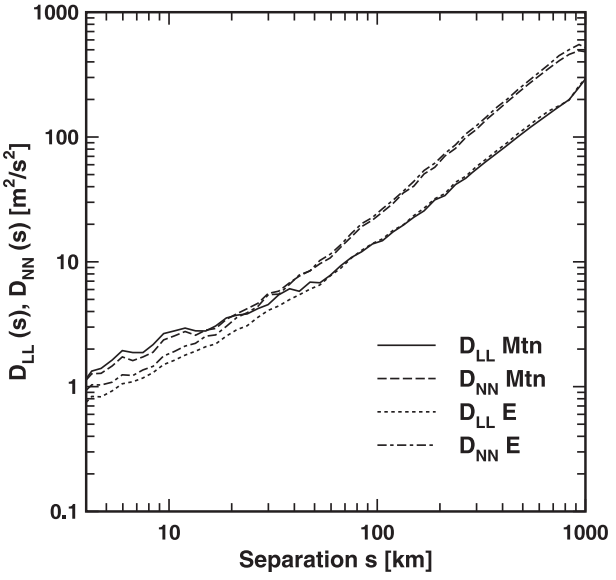

FIG. 14. Velocity structure functions D_{LL} and D_{NN} from the AMDAR data for the 250-hPa pressure level and latitude band of 30°–50°N for the Rocky Mountain region and the eastern United States.

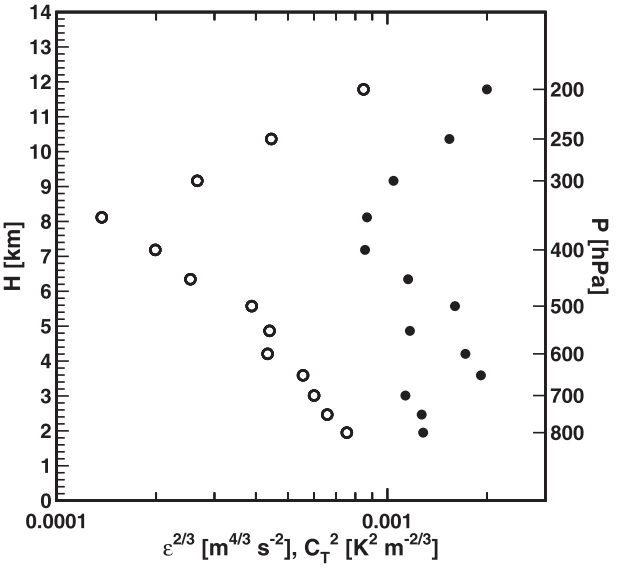

FIG. 15. Estimates of the small-scale turbulence statistics $\epsilon^{2/3}$ (filled circles) for the velocity field and C_T^2 (open circles) for the temperature field determined from the global AMDAR structure functions for the latitude band of 40°–50°N.

demonstrated that the $s^{2/3}$ scaling of D_{LL}, D_{NN}, and D_T extends to the smallest scales where the theory of homogeneous isotropic turbulence is valid [Tatarski 1967, his Eqs. (2.7) and (3.19), respectively]. Then,

$$D_{LL}(s) = C\epsilon^{2/3}s^{2/3} \quad \text{and} \tag{13}$$

$$D_T(s) = C_T^2 s^{2/3}, \tag{14}$$

where s is in meters and $C \approx 2.0$ is the Kolmogorov constant (Frisch 1995, p. 90). The AMDAR data resolve spatial scales of 10–50 km with sufficient statistical accuracy to produce a robust $s^{2/3}$ behavior. Consequently, Eqs. (13) and (14) can be used to derive reliable estimates of the average energy dissipation rate ϵ and structure constant C_T^2. Third-order structure functions can also be used to estimate ϵ but they have much larger statistical estimation error.

Comparing Eq. (13) with Eq. (10) gives $\epsilon^{2/3} = a_1/100C = a_1/200$ from D_{LL} and comparing Eq. (14) with Eq. (10) gives $C_T^2 = a_1/100$ from D_T. The coefficients a_1 ($m^2\ s^{-2}\ km^{-2/3}$) are listed in Tables A1–A10 of the appendix for various global and CONUS latitude bands and for various pressure levels. As an example, the vertical profiles of meridionally averaged $\epsilon^{2/3}$ and C_T^2 are shown in Fig. 15 for the 40°–50°N latitude band. A minimum in both the thermal (C_T^2) and velocity ($\epsilon^{2/3}$) turbulence levels occurs at ~8-km altitude, which reflects the lower average turbulence conditions above boundary layer convection and below the higher turbulence conditions associated with enhanced shear near the jet stream. Above this low-turbulence region the turbulence levels steadily increase to ~200 hPa, near the ceiling of most commercial aircraft. Comparison of the a_1 values in the tables of the appendix for other regions shows this vertical distribution is typical. Note that the structure functions at the lower altitudes (pressure greater than approximately 400 hPa; see Fig. 9) have a smaller $s^{2/3}$ regime than the Lindborg model based on typical aircraft cruising altitudes of 9–11 km. The scatter in the data at lower altitudes in Fig. 15 are produced by the smaller number of observations at the small lags and from the contribution from random outliers, which are difficult to identify because of the large tails in the distribution of the velocity and temperature differences (Figs. 3, 4).

These values of ϵ and C_T^2 are consistent with previous global estimates [e.g., in Fig. 15 at 10-km elevation, $\epsilon^{2/3} \approx 1.4 \times 10^{-3}\ m^{4/3}\ s^{-2}$ or $\epsilon \approx 5.2 \times 10^{-5}\ m^2\ s^{-3}$, which agrees with $\epsilon \approx 7.64 \times 10^{-5}\ m^2\ s^{-3}$ from Lindborg (1999) and $\epsilon^{2/3} \approx 1.7 \times 10^{-3}\ m^{4/3}\ s^{-2}$ for the 30°–50°N latitude region from Cho and Lindborg (2001, their Table 1)]. Similarly, at 10 km, $C_T^2 \approx 4 \times 10^{-4}\ K^2\ m^{-2/3}$ agrees with $C_T^2 \approx 5 \times 10^{-4}\ K^2\ m^{-2/3}$ determined by Frehlich and Sharman (2004) using the Nastrom and Gage (1985) GASP temperature spectra.

An early climatology of ϵ by Ellsaesser (1969) has a similar altitude dependence but the values are higher,

most likely a consequence of using large lags around 200 km that are not in the $s^{2/3}$ scaling region. Vinnichenko and Dutton (1969) present velocity spectra in the free atmosphere with the low-turbulence regime consistent with Fig. 15, but the high-turbulence values of ϵ are in excess of 0.01 $m^2\ s^{-3}$ (corresponding to "severe CAT"). Similar variations in ϵ were reported by Chen (1974). Profiles of ϵ from ground-based Doppler lidar have free-atmosphere values around $\epsilon \approx 1 \times 10^{-5}\ m^2\ s^{-3}$ (Frehlich et al. 2006; Frehlich and Kelley 2008), which agree with Fig. 15, but boundary layer values of ϵ can vary from as low as $1 \times 10^{-6}\ m^2\ s^{-3}$ for stable nighttime conditions to approximately 0.01 $m^2\ s^{-3}$ for convection (Frehlich et al. 1998, 2006) to as much as 0.1 $m^2\ s^{-3}$ for high wind conditions (Frehlich and Kelley 2008). Still another source for comparisons is the climatology of turbulence derived from NWP model output, which predicts $\langle \epsilon^{2/3} \rangle = 1.7 \times 10^{-3}\ m^{4/3}\ s^{-2}$ for an altitude of 10 km (Frehlich and Sharman 2004), which again is in good agreement with Fig. 15.

Other three-dimensional estimates of turbulence climatology have been attempted by Jaeger and Sprenger (2007) using 40-yr European Centre for Medium-Range Weather Forecasts (ECMWF) Re-Analysis (ERA-40) data and by Wolff and Sharman (2008) using pilot reports (PIREPS) of turbulence. However, both of these techniques are somewhat unreliable given the uncertainty in turbulence diagnostic formulations and model data used in the former and the subjective nature of PIREPs in the latter. Neither technique provides quantitative estimates of turbulence intensity.

Another point of comparison is inferences of ϵ and C_T^2 from radar measurements of spectral width or profiles of refractivity (e.g., Gage et al. 1980; Fukao et al. 1994; Cohn 1995; Hocking 1996; Nastrom and Eaton 1997, 2005; Satheesan and Krishna Murthy 2002; Masciadri and Egner 2006) or from stability profiles derived from high-resolution rawinsonde data (e.g., Bertin et al. 1997; Clayson and Kantha 2008). However, these are usually based on individual cases and tend to have large scatter.

Climatological studies of radar-derived ϵ and C_T^2 have been performed, but they are tied to a particular geographic location. Longer records of radar-derived ϵ (4 yr in the United States) by Nastrom and Eaton (1997) over White Sands, New Mexico, and Nastrom and Eaton (2005) over Vandenberg Air Force Base, California, have similar shapes. Similar results were produced by Fukao et al. (1994) over Japan. In comparing these results, it should be noted that the inference of ϵ from radar statistics is not straightforward, and involves a number of assumptions (Hocking 1996; Cohn 1995) regarding the nature of atmospheric turbulence in the free atmosphere, which may increase the uncertainty associated with radar-derived turbulence metrics. Our estimates of ϵ and C_T^2 are more directly tied to actual wind and temperature measurements and have three-dimensional coverage, and therefore should be more reliable and more indicative of true climatologies than those provided by limited radar studies.

From Eq. (10), the level of the structure functions at small spacings s scales as $a_1 s^{2/3}$, where a_1 represents a_L, a_N, and C_T^2 for the longitudinal velocity, transverse velocity, and temperature structure functions, respectively. An important aspect the observed levels in assessing theories of mesoscale turbulence is the ratio of the kinetic energy spectrum $\Phi_{KE}(k)$ to the potential energy spectrum $\Phi_{PE}(k)$ (Gage and Nastrom 1986; Gage et al. 1986; Cot 2001; Lindborg 2005, 2006; Lindborg and Brethouwer 2007). For the higher wavenumbers with the $k^{-5/3}$ scaling corresponding to the $s^{2/3}$ scaling of the structure functions (the spectral level is proportional to the structure function constant a_1) (Cot 2001),

$$R(k) = \frac{\Phi_{KE}(k)}{\Phi_{PE}(k)} = \frac{N^2 T_0^2 (a_L + a_N)}{g^2 C_T^2} \tag{15}$$

is independent of k, where T_0 is the average absolute temperature, g is the acceleration of gravity, and $N^2 = (g/\theta)(\partial\theta/\partial z)$ where θ is the mean potential temperature, z is the vertical direction, and N is the Brunt–Väisälä frequency. Since vertical gradients cannot be estimated from the AMDAR data, $N(z)$ is calculated from the U.S. Standard Atmosphere. The ratio R is tabulated in Table 1 for a few chosen altitudes in the troposphere and one in the stratosphere. Note that R is not constant with altitude but varies from approximately 1 to 2 with the highest values in the stratosphere (200 hPa). A similar enhancement in the stratosphere was produced by analyses of high-rate balloon data (Nastrom et al. 1997) but R was approximately a factor of 2 higher. Our magnitudes of R are consistent with other estimates from theory, observations, and numerical simulations of stratified and rotating turbulence. For example,

TABLE 1. Altitude dependence of energy spectral ratio R in latitude band 40°–50°N.

P (hPa)	H (km)	T (K)	θ (K)	$N^2 \times 10^{-4}$	R
500	5.605	251.7	307.3	1.27	1.51
400	7.223	241.3	313.9	1.33	1.81
300	9.200	228.4	322.6	1.40	1.36
250	10.407	220.6	328.4	1.45	1.03
200	11.830	216.7	343.7	4.41	2.02

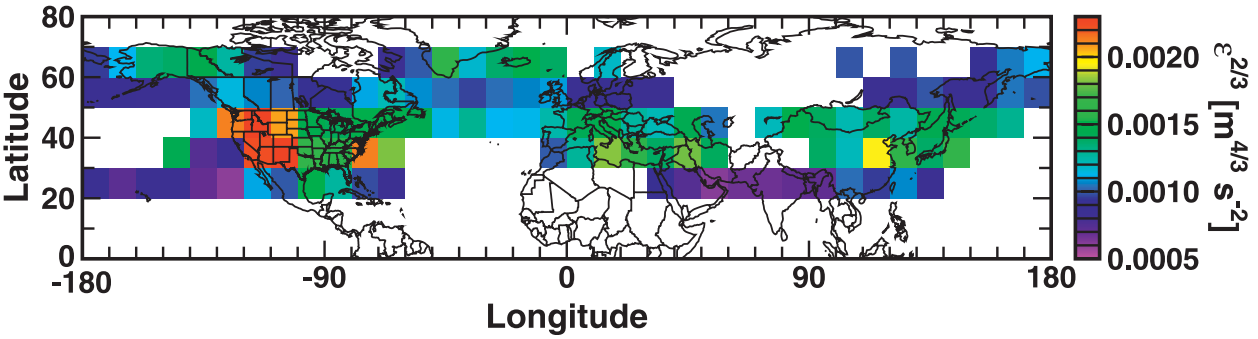

FIG. 16. Estimates of the small-scale turbulence statistics $\epsilon^{2/3}$ from AMDAR structure functions for 10° latitude–longitude boxes at the 250-hPa pressure level over NH.

$R = 2$ was proposed by Charney (1971) for geostrophic turbulence, and for plane inertia–gravity waves propagating in a constant wind and stability environment $R \geq 1$, where the lower limit of unity corresponds to no rotation (Gill 1989; Nappo 2002). Gage and Nastrom (1986; Gage et al. 1986) found $R \approx 2$ based on the GASP data. Lindborg (2006) produced a ratio ($R = \epsilon_K/\epsilon_P$ in his notation) that varied from 2.45 to 3.16 from numerical simulations of stratified turbulence. Including rotation in the simulations, Lindborg (2005) produced ratios that varied from 1.67 to 2.33. The ratios from Lindborg and Brethouwer (2007) varied from 1.7 to 3.1.

A map of average $\epsilon^{2/3}$ determined from all the AMDAR-derived velocity structure functions for 10° latitude–longitude boxes at 250 hPa for the Northern Hemisphere is shown in Fig. 16. There is a pronounced maximum over the Rocky Mountains (see Fig. 14), consistent with previous results (Nastrom and Gage 1985; Jasperson et al. 1990; Jaeger and Sprenger 2007; Wolff and Sharman 2008). The maximum off the southeast coast of the United States was also found in Wolff and Sharman (2008). The other elevated turbulence region over Asia is consistent with Jaeger and Sprenger (2007).

g. *Comparison with NWP model output*

Average velocity and temperature structure functions derived from the archive of the RUC13 analyses (interpolated to the RUC20 grid) for the years 2005 and 2006 are compared with the soundings/AMDAR average structure functions calculated over the same spatial domain in Fig. 17. The agreement between the two estimates for scales larger than 400 km is better than 10%, which indicates a robust climatology with just 2 yr of NWP model output. Similar results were produced from a 1-yr analysis of the Global Forecast System (GFS) output (not shown).

5. Summary and discussion

Structure functions [Eq. (1)] are easily computed from routine measurements of wind and temperature provided by the global AMDAR and rawinsonde observations, and allow computation of turbulence levels without recourse to data provided through special sampling programs such as GASP and MOZAIC. The large archive of rawinsonde and AMDAR data samples the 5–10 000-km spatial scales of atmospheric processes with acceptable accuracy for northern latitudes. Spatial scales less than 100 km are the most challenging since small observation errors or random outliers can have a large impact on the long-term averages (see Figs. 3, 4) and therefore careful QC of the data is required. Nevertheless, structure function shapes and levels were found to be very robust for scales as small as 2 km for velocity and 10 km for temperature. It was found that the statistics from the sounding data are more accurate for the larger scales while the AMDAR data provide better estimates at the smaller scales. Good agreement is produced in the overlap scales of 200–500 km (Figs. 5, 6) even though the spatial and temporal averages of the two data sources are quite different. Thus the combination of rawinsonde/AMDAR data to derive structure functions produces a complete description for all scales greater than ~5 km (see Figs. 7, 8). Empirical models [Eq. (10)] are fit to the merged structure functions for all regions that have sufficient statistical accuracy (see appendix).

Examples of the altitude dependence of the structure functions are shown in Fig. 9 and of latitude dependence in Fig. 10. The Lindborg model for the velocity structure functions is in good agreement with the results for the 250-hPa pressure level and the 40°–50°N latitude band (Fig. 7), which contains the largest number of commercial aircraft flights. There is a noticeable seasonal dependence at 30°–40°N and 250 hPa (Fig. 12), with more energy at the larger scales in the winter season. For the same region, there is good agreement at the mesoscales

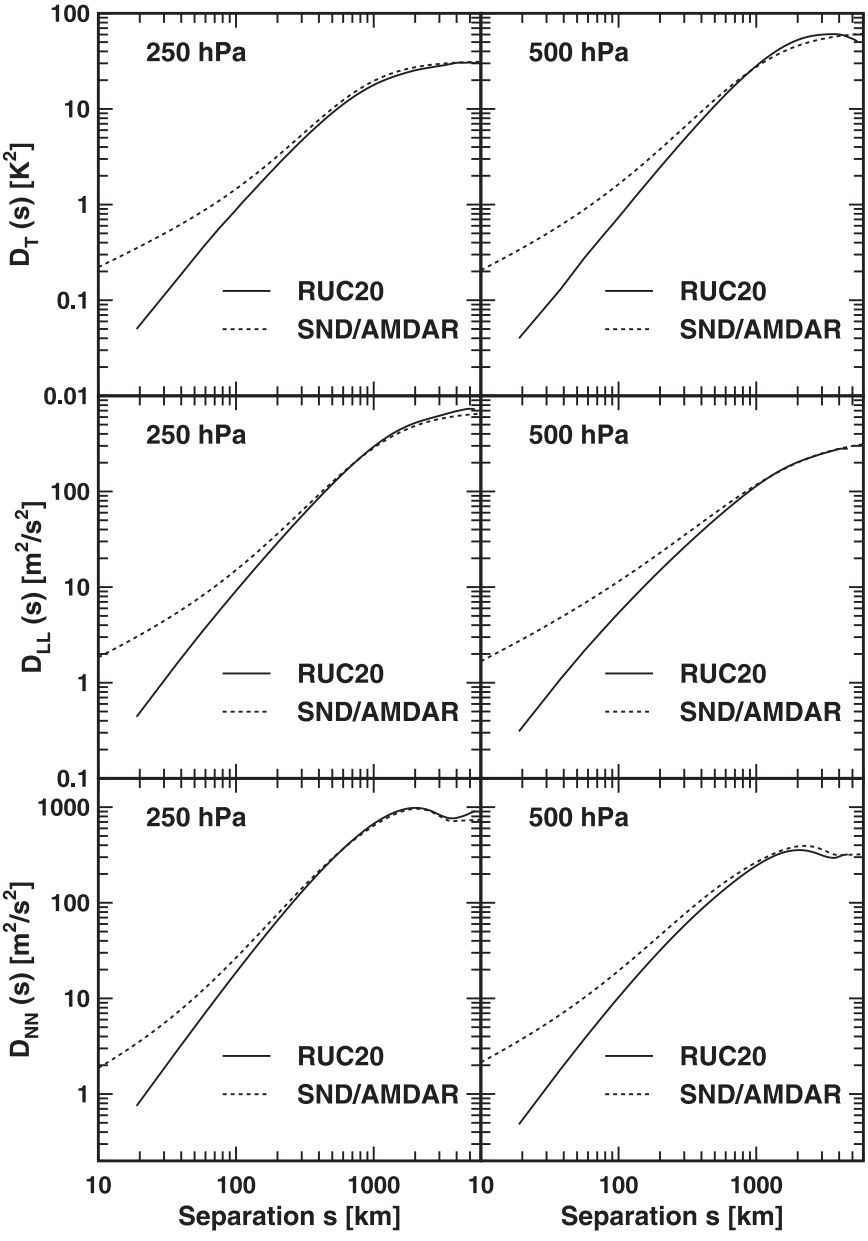

FIG. 17. Best-fit longitudinal velocity *LL*, transverse velocity *NN*, and temperature *T* structure functions for the AMDAR and SND compared with results from RUC20 for the 250- and 500-hPa pressure levels and the latitude band of 40°–50°N.

for the CONUS and Eurasian continent but with different behavior of the velocity statistics at the planetary scales. The different behavior of the structure functions at larger scales (greater than 2000 km) is partly related to the high density of data over the continents (Fig. 1) and therefore does not produce a true global average.

The leading-order scaling $s^{2/3}$ of the empirical model for the structure functions of velocity and temperature can be used to produce profiles of the small-scale turbulence statistics $\epsilon^{2/3}$ and C_T^2. The minimum of the turbulence levels at an altitude of 8 km (400 hPa) for the 40°–50°N latitude band reflects the lower turbulence region below the jet stream and above the convective boundary layer. This climatology of smaller-scale turbulence may provide useful connections to scales of turbulence that impact aviation safety (Wolff and Sharman 2008).

Our derived profiles of $\epsilon^{2/3}$ and C_T^2 predict the ratio R of kinetic energy to potential energy in the $k^{-5/3}$ region for the spatial spectra [Eq. (15); Gage and Nastrom 1986;

Gage et al. 1986; Cot 2001; Lindborg 2005, 2006; Lindborg and Brethouwer 2007], assuming the Brunt–Väisälä frequency N is a constant determined from the U.S. Standard Atmosphere. The ratio varied from 1.0 to 2.0, which is consistent with some past results and theoretical predictions, but the assumption of constant N requires more investigation since local regions of high turbulence would be expected to produce small or even negative values of N^2 (e.g., Bertin et al. 1997), which could bias the ratio R. Including the effects of random variations in N requires an appropriate spatial averaging domain for estimates of the θ gradients (Reiter and Lester 1968; Balsley et al. 2007).

The climatology of turbulence will improve as more and better data are archived, especially for the smaller scales, which are most sensitive to random measurement errors and outliers. This climatology is essential for a rigorous evaluation of the effective spatial resolution of NWP models (Frehlich and Sharman 2004, 2008), for correct interpretation of forecast error statistics or innovation statistics (Frehlich 2008), and for optimal data assimilation (Frehlich 2006; Frehlich and Sharman 2004). Further, knowledge of the climatology of turbulence permits more accurate calculations of the total observation errors and forecast errors. Total observation errors consist of two components (Frehlich 2001): the instrument error and the observation sampling error (related to the error of representativeness), which defines the errors produced by the mismatch between the observation sampling volume and the definition of ''truth.'' The most precise definition of truth for a given NWP model is the convolution of the continuous atmospheric field by the spatial filter of the NWP model (Frehlich 2006, 2008). Rawinsonde data have the largest observation sampling error since the sampling volume is very small (i.e., it is approximately a single point in the 2D horizontal plane). The average structure function and the spatial filter of the NWP model then determine the average observation sampling error (Frehlich 2001) as well as the atmospheric contribution to the average forecast errors, also called innovation errors (Frehlich 2008). For example, considering the latitude region 40°–50°N and a global model with grid resolution $\Delta = 35$ km and effective model resolution $L = 150$ km, the observation sampling error at 250 hPa for rawinsonde observations at the center of a grid cell for one horizontal velocity component is 1.61 m s^{-1} [Frehlich 2001, his Eq. (93)], which is larger than the instrument error of $\approx$0.5 m s^{-1}. In contrast, the observation sampling error for a rawinsonde temperature measurement is 0.50 K, which is comparable to the instrument error of 0.5 K.

Last, note that, as more and more aircraft become AMDAR equipped, it may be feasible to compute structure functions locally in real time and thus infer locations of elevated turbulence levels and provide new tools for turbulence detection and aviation safety (Wolff and Sharman 2008).

Acknowledgments. We thank Bill Moninger, NOAA/ESRL/GSD, for supplying us with the quality controlled AMDAR data and for his helpful comments on the data. We also thank Teddie Keller for useful comments and suggestions on an earlier version of the manuscript. This work was funded in part by NSF Grants ATM0646401 and ATM0522004, ARO Grant W911NF-06-1-0256, and by NASA ROSES Grant NNX08AL89G. We appreciate the very helpful comments of Erik Lindborg and the anonymous reviewers.

APPENDIX

Coefficients of Best-Fit Models

The coefficients of the best-fit models [Eq. (10)] for the global-averaged structure functions are given in Tables A1–A10 for the Northern Hemisphere using the merging technique shown in Figs. 7 and 8, except for the temperature structure functions in the latitude bands less than 20°N, which are based on the AMDAR data only. In Eq. (10), the variable s has units of kilometers, and consequently a_1 has units of $m^2\ s^{-2}\ km^{-2/3}$, a_2, a_4, and c_i have units of kilometers, a_3 is unitless, and b_i has units of meters squared per second squared.

TABLE A1. Coefficients for best fit to structure functions in 10°S–10°N.

Var	P (hPa)	H (km)	a_1	a_2	a_3	a_4
v_L	500	5.866	0.408 10	24.016	0.215 92	1304.7
v_L	400	7.584	0.225 52	2013.7	1.4445	3278.5
v_L	300	9.692	0.116 47	47.212	1.0289	3905.0
v_L	250	10.957	0.128 93	7.1911	0.897 23	8207.3
v_L	200	12.437	0.153 50	6.6815	0.910 17	14 392.0
v_N	500	5.866	0.354 28	830.73	5.4073	834.60
v_N	400	7.584	0.277 54	478.42	3.1042	623.86
v_N	300	9.692	0.229 89	139.41	1.5275	568.47
v_N	250	10.957	0.328 10	356.15	1.3696	1014.5
v_N	200	12.437	0.396 01	417.24	1.5493	1089.5
T	500	5.869	0.018 29	472.53	0.948 03	938.23
T	400	7.586	0.013 62	504.45	0.619 62	1993.8
T	300	9.694	0.008 43	213.81	0.843 42	3897.0
T	250	10.962	0.008 40	358.52	0.843 87	4363.2
T	200	12.439	0.013 34	1670.0	2.2114	2042.1

TABLE A2. Coefficients for best fit to structure functions in 10°–20°N.

Var	P (hPa)	H (km)	a_1	a_2	a_3	a_4
v_L	700	3.152	0.180 89	37 850.0	0.682 56	19 011.0
v_L	500	5.867	0.373 95	0.816 27	0.674 12	2381.4
v_L	400	7.580	0.149 48	158.47	1.3692	2001.8
v_L	300	9.681	0.171 30	141.27	1.4309	2001.7
v_L	250	10.943	0.094 13	8.3477	1.1229	3411.9
v_L	200	12.419	0.070 60	1.4620	1.0503	5744.1
v_N	700	3.152	0.316 25	519.85	3.5645	631.52
v_N	500	5.867	0.415 51	715.51	13.006	742.06
v_N	400	7.580	0.208 51	96.831	2.4898	303.55
v_N	300	9.681	0.276 57	202.56	2.4424	572.08
v_N	250	10.943	0.251 75	110.99	2.0949	530.64
v_N	200	12.419	0.241 97	87.443	1.8370	642.77
T	500	5.868	0.021 12	99.836	0.607 81	4671.0
T	400	7.580	0.016 05	60.851	0.830 47	3143.2
T	300	9.681	0.011 25	231.29	1.2345	2557.4
T	250	10.944	0.012 31	347.70	1.6430	1394.2
T	200	12.420	0.009 30	138.94	1.3730	1424.6

TABLE A3. Coefficients for best fit to structure functions in 20°–30°N.

Var	P (hPa)	H (km)	a_1	a_2	a_3	a_4
v_L	700	3.132	0.245 95	206.75	1.1706	1441.3
v_L	500	5.831	0.389 18	934.16	1.5951	2185.3
v_L	400	7.532	0.192 30	64.457	1.3156	1680.6
v_L	300	9.619	0.183 25	74.913	1.5748	1381.9
v_L	250	10.878	0.214 08	102.39	1.7075	1310.2
v_L	200	12.356	0.211 24	76.512	1.5882	1438.5
v_N	700	3.132	0.352 45	141.07	2.1181	339.85
v_N	500	5.831	0.337 00	94.847	1.6166	463.21
v_N	400	7.532	0.274 41	75.967	1.8554	441.01
v_N	300	9.619	0.267 05	84.152	2.0573	501.21
v_N	250	10.878	0.285 83	85.331	2.1096	518.91
v_N	200	12.356	0.235 50	53.884	1.8865	569.13
T	700	3.132	0.027 63	89.143	1.7005	721.25
T	500	5.832	0.036 55	135.49	1.2890	1439.1
T	400	7.532	0.007 88	9.7564	1.3359	1341.9
T	300	9.619	0.014 59	141.18	1.5382	2673.2
T	250	10.880	0.011 69	90.379	1.4456	2909.4
T	200	12.358	0.017 05	130.07	1.4077	2172.8

TABLE A4. Coefficients for best fit to structure functions in 30°–40°N.

Var	P (hPa)	H (km)	a_1	a_2	a_3	a_4	b_1	c_1	b_2	c_2
v_L	700	3.093	0.451 68	1237.8	2.0937	1738.6				
v_L	500	5.730	0.453 96	554.45	1.6891	1780.4				
v_L	400	7.388	0.171 72	17.725	1.2423	1996.6				
v_L	300	9.417	0.240 44	58.004	1.5248	1659.9				
v_L	250	10.644	0.354 28	124.37	1.7187	1519.6				
v_L	200	12.096	0.396 36	159.22	1.6561	1855.5				
v_N	700	3.093	0.471 93	347.76	1.5080	672.27	21.684	3525.4	15.793	21 926.0
v_N	500	5.730	0.455 62	142.75	1.6096	599.78	42.978	3877.6	22.693	21 706.0
v_N	400	7.388	0.260 05	30.140	1.5283	510.77	66.569	3986.4	27.174	21 337.0
v_N	300	9.417	0.303 15	51.383	1.8801	484.04	101.89	4082.2	41.946	21 274.0
v_N	250	10.644	0.383 33	72.278	1.9589	578.08	92.231	3979.6		
v_N	200	12.096	0.397 47	94.692	1.9941	579.91	123.12	4161.2	39.824	21 749.0
T	700	3.096	0.047 29	199.86	1.8832	1178.7				
T	500	5.733	0.052 38	317.88	1.9818	1089.2				
T	400	7.391	0.027 97	134.67	1.8261	978.63				
T	300	9.420	0.025 26	192.53	2.1079	1017.6				
T	250	10.647	0.035 43	219.84	2.0353	1058.8				
T	200	12.100	0.059 18	321.47	1.5943	1833.0				

TABLE A5. Coefficients for best fit to structure functions in 40°–50°N.

Var	P (hPa)	H (km)	a_1	a_2	a_3	a_4	b_1	c_1
v_L	700	3.031	0.247 68	68.491	1.0190	2057.7		
v_L	500	5.605	0.299 76	147.74	1.5197	1269.3	27.524	14 304.0
v_L	400	7.223	0.180 77	36.090	1.5255	1034.1	50.441	14 798.0
v_L	300	9.200	0.222 43	44.329	1.6556	995.21	75.187	14 545.0
v_L	250	10.398	0.330 23	88.073	1.7362	1087.8	80.270	14 416.0
v_L	200	11.830	0.427 00	185.64	1.6594	1475.5	70.246	13 904.0
v_N	700	3.031	0.382 89	132.35	1.3060	813.09	16.112	3392.5
v_N	500	5.605	0.341 54	66.545	1.5371	737.75	46.247	3395.6
v_N	400	7.223	0.202 55	19.680	1.6307	557.55	64.239	3539.5
v_N	300	9.200	0.227 63	24.187	1.7537	583.28	103.17	3455.5
v_N	250	10.398	0.293 60	35.967	1.7489	656.01	127.67	3544.9
v_N	200	11.830	0.336 99	61.897	1.6133	908.50	111.47	3598.9
T	700	3.034	0.030 16	17.706	1.2973	1809.9		
T	500	5.612	0.035 62	112.87	1.6660	1379.2		
T	400	7.230	0.017 00	42.955	1.5979	1222.2		
T	300	9.209	0.025 17	113.47	1.7313	1051.0		
T	250	10.407	0.044 54	154.43	1.8430	901.85		
T	200	11.839	0.081 14	244.28	2.0144	1066.3		

TABLE A6. Coefficients for best fit to structure functions in 50°–60°N.

Var	P (hPa)	H (km)	a_1	a_2	a_3	a_4	b_1	c_1
v_L	700	2.960	0.565 73	1804.2	3.4773	2103.3		
v_L	500	5.492	0.255 16	107.87	1.5525	1333.4		
v_L	400	7.082	0.160 78	37.370	1.6211	1074.9		
v_L	300	9.027	0.174 55	31.453	1.6619	1025.4		
v_L	250	10.210	0.201 09	38.272	1.5894	1234.5		
v_L	200	11.637	0.249 15	87.643	1.4986	1661.9		
v_N	700	2.960	0.634 16	533.19	2.1400	934.41	24.618	4186.9
v_N	500	5.492	0.277 11	55.858	1.6464	731.02	68.535	3887.0
v_N	400	7.082	0.173 50	18.203	1.6655	619.07	96.072	3773.9
v_N	300	9.027	0.157 41	14.033	1.7253	600.58	134.06	3646.5
v_N	250	10.210	0.176 57	18.024	1.6632	734.89	152.78	3617.1
v_N	200	11.637	0.202 93	36.092	1.5402	1038.1	118.89	3866.5
T	700	2.963	0.049 22	210.55	1.9228	1310.1	17.624	12 464.0
T	500	5.498	0.019 88	42.548	1.6160	1458.2		
T	400	7.090	0.013 33	31.609	1.6272	1372.5		
T	300	9.037	0.013 91	18.074	1.3292	1575.6		
T	250	10.221	0.038 62	80.515	1.6308	950.78		
T	200	11.646	0.070 01	169.40	2.0275	978.53		

TABLE A7. Coefficients for best fit to structure functions in 60°–70°N.

Var	P (hPa)	H (km)	a_1	a_2	a_3	a_4	b_1	c_1
v_L	700	2.879	0.662 73	1738.3	4.8263	1839.8		
v_L	500	5.369	0.712 71	709.04	2.6920	1208.8		
v_L	400	6.935	0.361 60	94.822	1.6537	1019.0		
v_L	300	8.855	0.216 63	44.146	1.7087	941.28		
v_L	250	10.030	0.259 61	72.516	1.7018	1088.2		
v_L	200	11.463	0.356 17	303.58	1.8892	1354.9		
v_N	700	2.879	0.809 06	773.79	2.7524	980.85	18.076	3913.0
v_N	500	5.369	0.571 44	187.04	2.0899	653.98	45.117	3903.6
v_N	400	6.935	0.266 96	21.394	1.6079	566.71	76.619	3785.5
v_N	300	8.855	0.156 77	11.293	1.5799	720.64	126.16	3282.4
v_N	250	10.030	0.230 43	31.161	1.6439	824.50	120.38	3496.4
v_N	200	11.463	0.329 21	125.84	1.7473	998.70	74.461	4108.2
T	700	2.879	0.037 44	218.68	2.5178	913.81	15.450	10 028.0
T	500	5.372	0.021 06	19.970	1.3963	1971.4		
T	400	6.939	0.028 41	104.85	1.8243	1226.6		
T	300	8.859	0.037 84	107.10	1.4825	1259.9		
T	250	10.035	0.064 53	167.46	2.0497	776.36		
T	200	11.466	0.091 10	286.83	2.2202	1047.8		

TABLE A8. Coefficients for best fit to structure functions over CONUS in 30°–40°N.

Var	P (hPa)	H (km)	a_1	a_2	a_3	a_4	b_1	c_1
v_L	700	3.112	0.406 98	10 324.0	1.0570	12 576.0		
v_L	500	5.761	0.440 15	820.28	1.2819	8203.9		
v_L	400	7.425	0.139 48	5.5361	1.0972	6539.4		
v_L	300	9.460	0.249 34	59.498	1.4867	1909.6		
v_L	250	10.687	0.363 19	129.40	1.7084	1540.4		
v_L	200	12.134	0.422 73	180.36	1.7040	1674.0		
v_N	700	3.112	0.380 64	324.41	1.0408	1935.1	32.932	3676.7
v_N	500	5.761	0.408 41	98.604	1.2496	1349.1	61.376	3908.2
v_N	400	7.425	0.184 64	9.0130	1.3042	885.68	82.518	4025.6
v_N	300	9.460	0.293 14	46.789	1.7567	683.80	105.35	4113.6
v_N	250	10.687	0.391 35	76.370	1.9174	684.16	114.46	4125.4
v_N	200	12.134	0.404 56	94.861	1.8654	798.90	99.195	3927.3
T	700	3.112	0.049 48	209.04	2.1186	1060.7		
T	500	5.766	0.064 83	495.72	2.3936	1077.6		
T	400	7.432	0.027 66	155.20	1.8162	1073.5		
T	300	9.469	0.023 29	189.60	1.9225	1068.0		
T	250	10.699	0.035 41	243.82	1.9630	899.36		
T	200	12.147	0.062 09	321.32	1.9628	1092.0		

TABLE A9. Coefficients for best fit to structure functions over CONUS in 40°–50°N.

Var	P (hPa)	H (km)	a_1	a_2	a_3	a_4	b_1	c_1
v_L	700	3.025	0.184 41	11.949	0.914 57	6084.6		
v_L	500	5.614	0.325 00	171.90	1.4382	2052.0		
v_L	400	7.241	0.241 15	59.000	1.5395	1379.3		
v_L	300	9.232	0.244 31	47.299	1.6040	1345.1		
v_L	250	10.438	0.370 49	109.09	1.7680	1312.4		
v_L	200	11.875	0.436 41	182.70	1.6886	1649.9		
v_N	700	3.025	0.315 18	75.834	1.1184	1703.1	36.337	3547.2
v_N	500	5.614	0.411 97	84.161	1.6648	788.12	53.693	4056.0
v_N	400	7.241	0.256 49	24.395	1.6008	723.00	90.544	3972.8
v_N	300	9.232	0.242 79	24.345	1.6945	790.29	145.76	3683.2
v_N	250	10.438	0.337 12	45.371	1.7892	816.29	163.20	3755.6
v_N	200	11.875	0.351 98	66.918	1.6735	1036.5	145.14	3864.0
T	700	3.029	0.020 56	12.849	1.4302	1665.9		
T	500	5.616	0.041 24	115.16	1.7241	1312.0		
T	400	7.244	0.026 79	92.839	1.7127	1444.7		
T	300	9.235	0.026 72	147.32	1.7838	1201.5		
T	250	10.442	0.046 49	180.55	1.9179	887.94		
T	200	11.879	0.082 33	278.48	2.1709	1078.1		

TABLE A10. Coefficients for best fit to structure functions over CONUS in 50°–60°N.

Var	P (hPa)	H (km)	a_1	a_2	a_3	a_4	b_1	c_1
v_L	700	2.933	0.186 69	10.363	0.989 13	2310.9		
v_L	500	5.458	0.029 18	0.694 88	1.2489	1593.8		
v_L	400	7.046	0.174 31	45.058	1.6889	1025.0		
v_L	300	8.991	0.199 38	33.074	1.6355	1139.4		
v_L	250	10.178	0.203 35	34.152	1.5639	1383.9		
v_L	200	11.616	0.270 01	97.018	1.5605	1597.8		
v_N	700	2.933	0.278 31	9.6242	1.0473	1306.2		
v_N	500	5.458	0.097 40	3.1345	1.2321	1358.6	69.657	3279.8
v_N	400	7.046	0.060 12	2.2407	1.4277	856.66	97.881	3316.0
v_N	300	8.991	0.175 16	14.323	1.6598	710.23	130.39	3427.0
v_N	250	10.178	0.204 32	21.473	1.6538	819.66	139.56	3420.9
v_N	200	11.616	0.225 25	43.164	1.5736	1053.9	102.71	3772.0
T	700	2.934	0.065 62	133.10	1.8109	1309.6		
T	500	5.460	0.022 87	39.097	1.5667	1810.5		
T	400	7.049	0.024 99	81.728	1.7707	1460.1		
T	300	8.995	0.034 06	147.00	1.7227	1200.5		
T	250	10.183	0.052 99	169.49	2.0041	858.43		
T	200	11.621	0.073 61	182.31	1.9701	1068.0		

REFERENCES

Ballish, B. A., and V. K. Kumar, 2008: Systematic differences in aircraft and radiosonde temperatures. *Bull. Amer. Meteor. Soc.,* **89,** 1689–1707.

Balsley, B. B., G. Svensson, and M. Tjernstrom, 2007: On the scale-dependence of the gradient Richardson number in the residual layer. *Bound.-Layer Meteor.,* **127,** 57–72.

Barnes, S. L., and D. K. Lilly, 1975: Covariance analysis of severe storm environments. Preprints, *Ninth Conf. on Severe Local Storms,* Norman, OK, Amer. Meteor. Soc., 301–306.

Bengtsson, L., S. Hagemann, and K. I. Hodges, 2004: Can climate trends be calculated from reanalysis data? *J. Geophys. Res.,* **109,** D11111, doi:10.1029/2004JD004536.

Benjamin, S. G., B. E. Schwartz, and R. E. Cole, 1999: Accuracy of ACARS wind and temperature observations determined by collocation. *Wea. Forecasting,* **14,** 1032–1038.

Benton, G. S., and A. B. Kahn, 1958: Spectra of large-scale atmospheric flow at 300 millibars. *J. Atmos. Sci.,* **15,** 404–410.

Bertin, F., J. Barat, and R. Wilson, 1997: Energy dissipation rates, eddy diffusivity, and the Prandtl number: An in situ experimental approach and its consequences on radar estimate of turbulent parameters. *Radio Sci.,* **32,** 791–804.

Buell, C. E., 1960: The structure of two-point wind correlations in the atmosphere. *J. Geophys. Res.,* **65,** 3353–3366.

Charney, J. G., 1971: Geostrophic turbulence. *J. Atmos. Sci.,* **28,** 1087–1095.

Chen, W. Y., 1974: Energy dissipation rates of the free atmospheric turbulence. *J. Atmos. Sci.,* **31,** 2222–2225.

Cho, J. Y. N., and E. Lindborg, 2001: Horizontal velocity structure functions in the upper troposphere and lower stratosphere 1. Observations. *J. Geophys. Res.,* **106,** 10 223–10 232.

——, R. E. Newell, and J. D. Barrick, 1999: Horizontal wavenumber spectra of winds, temperature, and trace gases during the Pacific Exploratory Missions: 2. Gravity waves, quasi-two-dimensional turbulence, and vortical modes. *J. Geophys. Res.,* **104,** 16 297–16 308.

Clayson, C. A., and L. Kantha, 2008: On turbulence and mixing in the free atmosphere inferred from high-resolution soundings. *J. Atmos. Oceanic Technol.,* **25,** 833–852.

Cohn, S. A., 1995: Radar measurements of turbulent eddy dissipation rate in the troposphere: A comparison of techniques. *J. Atmos. Oceanic Technol.,* **12,** 85–95.

Cot, C., 2001: Equatorial mesoscale wind and temperature fluctuations in the lower atmosphere. *J. Geophys. Res.,* **106,** 1523–1532.

Drüe, C., W. Frey, A. Hoff, and Th. Hauf, 2008: Aircraft type-specific errors in AMDAR weather reports from commercial aircraft. *Quart. J. Roy. Meteor. Soc.,* **134,** 229–239.

Ellsaesser, H. W., 1969: A climatology of epsilon (atmospheric dissipation). *Mon. Wea. Rev.,* **97,** 415–423.

Fil, C., and L. Dubus, 2005: Winter climate regimes over the North Atlantic and European region in ERA40 reanalysis and DEMETER seasonal hindcasts. *Tellus,* **57,** 290–307.

Frehlich, R., 2001: Errors for space-based Doppler lidar wind measurements: Definition, performance, and verification. *J. Atmos. Oceanic Technol.,* **18,** 1749–1772.

——, 2006: Adaptive data assimilation including the effect of spatial variations in observation error. *Quart. J. Roy. Meteor. Soc.,* **132,** 1225–1257.

——, 2008: Atmospheric turbulence component of the innovation covariance. *Quart. J. Roy. Meteor. Soc.,* **134,** 931–940.

——, and R. Sharman, 2004: Estimates of turbulence from numerical weather prediction model output with applications to turbulence diagnosis and data assimilation. *Mon. Wea. Rev.,* **132,** 2308–2324.

——, and ——, 2008: The use of structure functions and spectra from numerical model output to determine effective model resolution. *Mon. Wea. Rev.,* **136,** 1537–1553.

——, and N. Kelley, 2008: Measurements of wind and turbulence profiles with scanning Doppler lidar for wind energy applications. *IEEE J. Sel. Top. Appl. Earth Obs. Remote Sens.,* **1,** 42–47.

——, S. Hannon, and S. Henderson, 1998: Coherent Doppler lidar measurements of wind field statistics. *Bound.-Layer Meteor.,* **86,** 233–256.

——, Y. Meillier, M. L. Jensen, B. Balsley, and R. Sharman, 2006: Measurements of boundary layer profiles in an urban environment. *J. Appl. Meteor. Climatol.,* **45,** 821–837.

Frisch, U., 1995: *Turbulence, the Legacy of A. N. Kolmogorov*. Cambridge University Press, 296 pp.

Fukao, S., and Coauthors, 1994: Seasonal variability of vertical eddy diffusivity in the middle atmosphere: 1. Three-year observations by the middle and upper atmosphere radar. *J. Geophys. Res.,* **99,** 18 973–18 987.

Gage, K. S., and G. D. Nastrom, 1986: Theoretical interpretation of atmospheric wavenumber spectra of wind and temperature observed by commercial aircraft during GASP. *J. Atmos. Sci.,* **43,** 729–740.

——, J. L. Green, and T. E. VanZandt, 1980: Use of Doppler radar for the measurement of atmospheric turbulence parameters from the intensity of clear-air echoes. *Radio Sci.,* **15,** 407–416.

——, ——, and ——, 1986: Spectrum of atmospheric vertical displacements and spectrum of conservative scalar passive additives due to quasi-horizontal atmospheric motions. *J. Geophys. Res.,* **91,** 13 211–13 216.

Gill, A. E., 1989: *Atmosphere-Ocean Dynamics*. Academic Press, 662 pp.

Gkioulekas, E., and K. K. Tung, 2006: Recent developments in understanding two-dimensional turbulence and the Nastrom-Gage spectrum. *Low Temp. Phys.,* **145,** 25–57.

Gomis, D., and S. Alonso, 1988: Structure function responses in a limited area. *Mon. Wea. Rev.,* **116,** 2254–2264.

Grotjahn, R., 1993: *Global Atmospheric Circulations*. Oxford, 430 pp.

Hamilton, K., Y. O. Takahashi, and W. Ohfuchi, 2008: Mesoscale spectrum of atmospheric motions investigated in a very fine resolution global general circulation model. *J. Geophys. Res.,* **113,** D18110, doi:10.1029/2008JD009785.

Hocking, W. K., 1996: An assessment of the capabilities and limitations of radars in measurements of atmosphere turbulence. *Adv. Space Res.,* **17,** 37–47.

Hoinka, K. P., 1998: Statistics of the global tropopause pressure. *Mon. Wea. Rev.,* **126,** 3303–3325.

Hoskins, B. J., H. H. Hsu, I. N. James, M. Masutani, P. D. Sardeshmukh, and G. H. White, 1989: Diagnostics of the global atmospheric circulation based on ECMWF analyses 1979–1989. Tech. Rep. WCRP-27, WMO/TD-326, 217 pp. [Available from World Meteorological Organization, Case Postale 2300, CH-1211 Geneva 20, Switzerland.]

Jaatinen, J., and J. B. Elms, 2000: On the windfinding accuracy of Loran-C, GPS and radar. *Väisälä News,* **152,** 30–33.

Jaeger, E. B., and M. Sprenger, 2007: A northern-hemispheric climatology of indices for clear air turbulence in the tropopause region derived from ERA40 re-analysis data. *J. Geophys. Res.,* **112,** D20106, doi:10.1029/2006JD008189.

Jasperson, W. H., G. D. Nastrom, and D. C. Fritts, 1990: Further study of terrain effects on the mesoscale spectrum of atmospheric motions. *J. Atmos. Sci.,* **47,** 979–987.

Julian, P. R., and A. K. Cline, 1974: The direct estimation of spatial wavenumber spectra of atmospheric variables. *J. Atmos. Sci.,* **31,** 1526–1539.

Kalnay, E., 2003: *Atmospheric Modeling, Data Assimilation and Predictability*. Cambridge University Press, 342 pp.

——, and Coauthors, 1996: The NCEP/NCAR 40-Year Reanalysis Project. *Bull. Amer. Meteor. Soc.,* **77,** 437–471.

Koch, P., H. Wernli, and H. W. Davies, 2006: An event-based jet-stream climatology and typology. *Int. J. Climatol.,* **26,** 283–301.

Koshyk, J. N., and K. Hamilton, 2001: The horizontal kinetic energy spectrum and spectral budget simulated by a high-resolution troposphere–stratosphere–mesosphere GCM. *J. Atmos. Sci.,* **58,** 329–348.

Lenschow, D. H., J. Mann, and L. Kristensen, 1994: How long is long enough when measuring fluxes and other turbulent statistics? *J. Atmos. Oceanic Technol.,* **11,** 661–673.

Lindborg, E., 1999: Can the atmospheric kinetic energy spectrum be explained by two-dimensional turbulence? *J. Fluid Mech.,* **388,** 259–288.

——, 2005: The effect of rotation on the mesoscale energy cascade in the free atmosphere. *Geophys. Res. Lett.,* **32,** L01809, doi:10.1029/2004GL021319.

——, 2006: The energy cascade in a strongly stratified fluid. *J. Fluid Mech.,* **550,** 207–242.

——, 2007: Horizontal wavenumber spectra of vertical vorticity and horizontal divergence in the upper troposphere and lower stratosphere. *J. Atmos. Sci.,* **64,** 1017–1025.

——, and J. Y. N. Cho, 2001: Horizontal velocity structure functions in the upper troposphere and lower stratosphere 2. Theoretical considerations. *J. Geophys. Res.,* **106,** 233–241.

——, and G. Brethouwer, 2007: Stratified turbulence forced in rotational and divergent modes. *J. Fluid Mech.,* **586,** 83–108.

Lorenz, E. N., 1967: The nature and theory of the general circulation of the atmosphere. WMO 218, TP 115, 161 pp.

Luers, J. K., 1997: Temperature error of the Väisälä RS90 radiosonde. *J. Atmos. Oceanic Technol.,* **14,** 1520–1532.

——, and R. E. Eskridge, 1998: Use of radiosonde temperature data in climate studies. *J. Climate,* **11,** 1002–1019.

Maddox, R. A., and T. H. Vonder Haar, 1979: Covariance analyses of satellite-derived mesoscale wind fields. *J. Appl. Meteor.,* **18,** 1327–1334.

Masciadri, E., and S. Egner, 2006: First seasonal study of optical turbulence with an atmospheric model. *Astron. Soc. Pac.,* **118,** 1604–1619.

Monin, A. S., and A. M. Yaglom, 1975: *Statistical Fluid Mechanics: Mechanics of Turbulence*. Vol. 2. MIT Press, 874 pp.

Moninger, W. R., R. D. Mamrosh, and P. M. Pauley, 2003: Automated meteorological reports from commercial aircraft. *Bull. Amer. Meteor. Soc.,* **84,** 203–216.

Nappo, C. J., 2002: *An Introduction to Atmospheric Gravity Waves*. Academic Press, 276 pp.

Nastrom, G. D., and K. S. Gage, 1985: A climatology at atmospheric wavenumber spectra of wind and temperature observed by commercial aircraft. *J. Atmos. Sci.,* **42,** 950–960.

——, and F. D. Eaton, 1997: Turbulence eddy dissipation rates from radar observations at 5–20 km at White Sands Missile Range, New Mexico. *J. Geophys. Res.,* **102,** 19 495–19 505.

——, and ——, 2005: Seasonal variability of turbulence parameters at 2 to 21 km from MST radar measurements at Vandenberg Air Force Base, California. *J. Geophys. Res.,* **110,** D19110, doi:10.1029/2005JD005782.

——, T. E. Van Zandt, and J. M. Warnock, 1997: Vertical wavenumber spectra of wind and temperature from high-resolution balloon soundings over Illinois. *J. Geophys. Res.,* **102,** 6685–6701.

Ogura, Y., 1952: The structure of two-dimensionally isotropic turbulence. *J. Meteor. Soc. Japan,* **30,** 59–64.

Palmen, E., and C. W. Newton, 1969: *Atmospheric Circulation Systems*. Elsevier, 603 pp.

Pauley, P. A., 2002: Telling north from south: An example of an error in automated aircraft data. *Wea. Forecasting,* **17,** 334–336.

Peters, M. E., Z. Kuang, and C. C. Walker, 2008: Analysis of atmospheric energy transport in ERA-40 and implications for simple models of the mean tropical circulation. *J. Climate,* **21,** 5229–5241.

Press, W. H., B. P. Flannery, S. A. Teukolsky, and W. T. Vetterling, 1986: *Numerical Recipes: The Art of Scientific Computing*. 2nd ed. Cambridge University Press, 963 pp.

Reiter, E. R., and P. F. Lester, 1968: Richardson's number in the free atmosphere. *Arch. Meteor. Geophys. Bioklimatol. Ser. A,* **17,** 1–7.

Riley, J. J., and E. Lindborg, 2008: Stratified turbulence: A possible interpretation of some geophysical turbulence measurements. *J. Atmos. Sci.,* **65,** 2416–2424.

Satheesan, K., and B. V. Krishna Murthy, 2002: Turbulence parameters in the tropical troposphere and lower stratosphere. *J. Geophys. Res.,* **107,** 4002, doi:10.1029/2000JD000146.

Skamarock, W. A., 2004: Evaluating mesoscale NWP models using kinetic energy spectra. *Mon. Wea. Rev.,* **132,** 3019–3032.

Takahashi, Y. O., K. Hamilton, and W. Ohfuchi, 2006: Explicit global simulation of the mesoscale spectrum of atmospheric motions. *Geophys. Res. Lett.,* **33,** L12812, doi:10.1029/2006GL026429.

Tatarski, V. I., 1967: *Wave Propagation in a Turbulent Medium*. Dover Publications, 285 pp.

Tulloch, R., and K. S. Smith, 2006: A theory for the atmospheric energy spectrum: Depth-limited temperature anomalies at the tropopause. *Proc. Natl. Acad. Sci. USA,* **103,** 14 690–14 694.

——, and ——, 2009: Quasigeostrophic turbulence with explicit surface dynamics: Application to the atmospheric energy spectrum. *J. Atmos. Sci.,* **66,** 450–467.

Tung, K. K., and W. W. Orlando, 2003: The k^3 and $k^{5/3}$ energy spectrum of atmospheric turbulence: Quasigeostrophic two-level model simulation. *J. Atmos. Sci.,* **60,** 824–835.

Uppala, S. M., and Coauthors, 2005: The ERA-40 Re-Analysis. *Quart. J. Roy. Meteor. Soc.,* **131,** 2961–3012.

Vinnichenko, N. K., and J. A. Dutton, 1969: Empirical studies of atmospheric structure and spectra in the free atmosphere. *Radio Sci.,* **4,** 1115–1126.

Wolff, J., and R. Sharman, 2008: Climatology of upper-level turbulence over the continental United States. *J. Appl. Meteor. Climatol.,* **47,** 2198–2214.